

# Reduced order modeling with time-dependent bases for PDEs with stochastic boundary conditions\*

Prerna Patil and Hessam Babaee

**Abstract.** Low-rank approximation using time-dependent bases (TDBs) has proven effective for reduced-order modeling of stochastic partial differential equations (SPDEs). In these techniques, the random field is decomposed to a set of deterministic TDBs and time-dependent stochastic coefficients. When applied to SPDEs with non-homogeneous stochastic boundary conditions (BCs), appropriate BC must be specified for each of the TDBs. However, determining BCs for TDB is not trivial because: (i) the dimension of the random BCs is different than the rank of the TDB subspace; (ii) TDB in most formulations must preserve orthonormality or orthogonality constraints and specifying BCs for TDB should not violate these constraints in the space-discretized form. In this work, we present a methodology for determining the boundary conditions for TDBs at no additional computational cost beyond that of solving the same SPDE with homogeneous BCs. Our methodology is informed by the fact the TDB evolution equations are the optimality conditions of a variational principle. We leverage the same variational principle to derive an evolution equation for the value of TDB at the boundaries. The presented methodology preserves the orthonormality or orthogonality constraints of TDBs. We present the formulation for both the dynamically bi-orthonormal (DBO) decomposition [1] as well as the dynamically orthogonal (DO) decomposition [2]. We show that the presented methodology can be applied to stochastic Dirichlet, Neumann, and Robin boundary conditions. We assess the performance of the presented method for linear advection-diffusion equation, Burgers' equation, and two-dimensional advection-diffusion equation with constant and temperature-dependent conduction coefficient.

**Key words.** Uncertainty quantification, time-dependent bases, stochastic boundary conditions, reduced order modeling, variational principle

**AMS subject classifications.** 68Q25, 68R10, 68U05

## 1. Introduction.

**1.1. Background.** The quantification of uncertainty in numerical models of real-world processes has gained significant traction in recent decades. The uncertainty in the numerical systems can arise out of random initial conditions, boundary conditions, imperfectly known model parameters, and input parameters. Uncertainty quantification (UQ) can rank the effect of different random sources on the quantities of interest and can be utilized to reduce uncertainty. Several techniques have been developed in the pursuit of performing UQ. Sampling-based techniques such as Monte-Carlo (MC), multi-level MC, quasi-MC (QMC), sequential MC [3–7] use discrete samples to represent the joint probability distribution of the response surface. These methods can be computationally prohibitive since a large number of samples are required to obtain a sufficient degree of accuracy. Another class of technique called the polynomial chaos expansion (PCE) is based on the Galerkin projection of the response onto a PCE [8–18]. The efficiency of PCE has been demonstrated for solving elliptic and low Reynolds number fluids problems [19–27]. PCE still requires a large number of samples for problems with high-dimensional random space. Moreover, the polynomial order must increase with time to keep same level of errors as demonstrated in the case of stochastic linear advection equation [28]. The method also shows a limitation in nonlinear systems with intermittency [29] and oscillatory stochastic processes [30].

\*This work has been funded by Air Force Office of Scientific Research award (PM: Fariba Faharoo), FA9550-21-1-0247 and by the National Science Foundation (NSF) USA, under grant no.2042918

**1.2. Time-dependent reduced order models.** One way to reduce the computational cost of performing UQ is to use stochastic reduced-order models (ROMs). ROMs are fast surrogate models that can reduce the computational cost by exploiting correlations of the system response between different random samples. A majority of the ROM techniques are data-driven, i.e., they require observations of the full order model, which may be expensive and are based on static subspaces, which can hamper their efficiency for highly transient problems. Reduced-order modeling based on a time-dependent basis (TDB) can potentially overcome some of the limitations of data-driven ROMs, in which data-generation can be completely eliminated and TDBs can chase the low-rank subspace instantaneously. Recent developments in the context of TDB to overcome the limitations imposed by fixed basis have led to the dynamically orthogonal (DO) method [2, 31, 32], in which the random field is decomposed to a set of orthonormal TDB and time-dependent stochastic coefficients. The orthonormality constraint imposed on TDB can be modified to obtain other decompositions, for example, bi-orthogonal (BO) decomposition [33, 34] and dynamically bi-orthonormal (DBO) decomposition [1]. It has been shown in [1, 35] that these three methods (DO, BO, DBO) are equivalent in the sense that their low-rank representations span the same subspace instantaneously and the difference between these methods correspond to an in-subspace rotation and scaling. The application of TDB is not limited to SPDEs. The TDB has been recently applied to deterministic problems for various applications, for example, reduced description of transient instabilities [36–39], flow control [40], prediction of extreme events [41], computing sensitivities [42], skeletal model reduction of detailed kinetics [43] as well as reduced-order modeling of passive and reactive species transport [44]. TDB has also been introduced independently in quantum mechanics, chemistry, dynamic low rank matrix and tensor approximations [45–48].

**1.3. Boundary conditions.** The majority of DO, BO, and DBO applications have focused on problems with either deterministic boundary conditions or very simple stochastic boundary conditions, e.g., homogeneous Neumann boundary conditions. The reason is that for stochastic boundary conditions with non-homogeneous Dirichlet, Neumann, or Robin type, it is not trivial how the stochasticity at the boundary should be distributed between different spatial modes and their stochastic coefficients. These challenges are further compounded by the fact that in any of the DO, BO, or DBO formulations, the spatial modes must satisfy either orthogonality or orthonormality constraints. This implies that a principled approach for determining the boundary conditions should incorporate global spatial state of the modes. An alternative approach was recently used in [49], by splitting the modes into two sets of homogeneous and non-homogeneous modes i.e., boundary modes, in which the stochastic Dirichlet boundary conditions are strongly enforced using the non-homogeneous modes. In this approach, the number of boundary modes is tied to the number of random dimension. As a result, for problems with high-dimensional random boundary conditions, the overall computational cost could be significant. Because of these challenges, the majority of SPDEs solved with DO, DBO or BO have homogeneous stochastic boundary conditions, while many realistic UQ problems are formulated as random-BC problems.

**1.4. Our contributions.** In this paper, we present a methodology to determine the boundary for the spatial modes for DO and DBO methodologies. We present a unified formulation for different types of stochastic boundary conditions, i.e., Dirichlet, Neumann and Robin. Our methodology is informed by the fact that the evolution equations of DO and DBO are the first-order optimality conditions of their respective variational principles. We present this variational formulation and show how boundary conditions can be incorporated into the variational problem in a principled manner. Using the variational principle, we derive an evolution equation for the value of the spatial modes at the boundary. Our approach does not add any additional computational cost beyond



that of solving the same SPDE with homogeneous BCs and its implementation is straightforward. The presented approach also satisfies the orthonormality or orthogonality constraints in a natural manner.

The paper is organized as follows: In section 2, the methodology and derivation of the equations is shown. In section 3, the method is applied to several benchmark problems: (i) linear advection-diffusion equation, (ii) Burgers' equation, (iii) two dimensional linear advection-diffusion equation and (iv) two dimensional nonlinear advection-diffusion equation. In section 4, the paper is concluded with a brief summary of the results.

## 2. Methodology.

**2.1. Definitions and notation.** In this section, we present the various definitions and notation used in this paper. A continuous function/variable and scalar is shown by non-bold letters ( $v$ ), vectors are shown using bold lowercase letters ( $\mathbf{v}$ ) and matrices are described using bold uppercase letters ( $\mathbf{V}$ ). We use MATLAB semi-colon convention to vertically append two matrices or vectors, i.e.,  $\mathbf{V} = [\mathbf{V}_1; \mathbf{V}_2]$ , where  $\mathbf{V}_1 \in \mathbb{R}^{n_1 \times d}$ ,  $\mathbf{V}_2 \in \mathbb{R}^{n_2 \times d}$  and  $\mathbf{V} \in \mathbb{R}^{(n_1+n_2) \times d}$ . We also denote the time derivative with  $(\dot{\sim}) = d(\sim)/dt$ .

We denote a random field by  $u(x, t; \omega)$ , where  $x \in \bar{D}$  denotes the spatial coordinates in the physical domain  $\bar{D} \subset \mathcal{R}^d$ , where  $d = 1, 2$  or  $3$ ,  $t > 0$  denotes the time and  $\omega$  denotes a random event in the sample space  $\Omega$ . We consider the following SPDE subject to random boundary and initial conditions:

$$(2.1) \quad \frac{\partial v(x, t; \omega)}{\partial t} = \mathcal{N}(v(x, t; \omega), t), \quad x \in D, \omega \in \Omega,$$

$$(2.2) \quad av(x, t; \omega) + b \frac{\partial v(x, t; \omega)}{\partial n} = g(x, t; \omega), \quad x \in \partial D, \omega \in \Omega,$$

$$(2.3) \quad v(x, t_0; \omega) = v_0(x; \omega), \quad x \in \bar{D}, \omega \in \Omega,$$

where  $\mathcal{N}(v(x, t; \omega), t)$  is in general, a nonlinear differential operator,  $D$  denotes the interior domain,  $\partial D$  denotes the boundary and  $\bar{D} = D \cup \partial D$ . We consider the above equation in the discrete form in the spatial domain ( $x$ ) and the random space ( $\omega$ ). In the space-discretized form,  $x$  is represented by  $\bar{\mathbf{x}} = [\mathbf{x}; \mathbf{x}_b]$ , where  $\mathbf{x}$  represents the points in the interior of the domain,  $\mathbf{x}_b$  represents the boundary points and  $\bar{\mathbf{x}} \in \mathbb{R}^{\bar{n} \times d}$ ,  $\mathbf{x} \in \mathbb{R}^{n \times d}$  and  $\mathbf{x}_b \in \mathbb{R}^{n_b \times d}$ . Here,  $n$  denotes the number of points in the interior domain ( $D$ ),  $n_b$  denotes the number of points on the boundary of the domain ( $\partial D$ ) and  $\bar{n}$  represents the total discrete points in the domain  $\bar{D}$ , where  $\bar{n} = n + n_b$ . A continuous function  $v(x)$  is shown in the discrete form by a vector  $\mathbf{v}_{\bar{\mathbf{x}}}$ , where  $\mathbf{v}_{\bar{\mathbf{x}}} \in \mathbb{R}^{\bar{n}}$ . The subscript denotes the value of the function at the  $\bar{\mathbf{x}}$  discrete points in the domain. The vector can be separated into two subsets,  $\mathbf{v}_{\bar{\mathbf{x}}} = [\mathbf{v}_{\mathbf{x}}; \mathbf{v}_{\mathbf{x}_b}]$ , which represent the value of the function at points in the interior domain given by  $\mathbf{v}_{\mathbf{x}}$  and value at points on the boundary  $\mathbf{v}_{\mathbf{x}_b}$ . We note that the discretization in the spatial domain can be performed using any method of choice, e.g., finite element method, finite volume method, spectral element method, etc, but for the sake of simplicity in notation, our methodology is presented for collocation-type discretizations, where the entries of vector  $\mathbf{v}_{\bar{\mathbf{x}}}$  represent the values of the solution at point  $\bar{\mathbf{x}}$ . In Eq.(2.2), we obtain three types of stochastic boundary conditions based on the values of  $a$  and  $b$ : (i) Dirichlet for  $b = 0, a \neq 0$  (ii) Neumann for  $a = 0, b \neq 0$  and (iii) Robin for  $a \neq 0, b \neq 0$ .

The random space is also considered in the discretized form. We consider that random samples of  $\omega$  are drawn and therefore, a random number  $y(\omega)$  is represented as a vector of samples  $\mathbf{y}$  and  $\mathbf{y} \in \mathbb{R}^{n_s}$  where  $n_s$  denotes the number of samples. The sampling in the random space can be

performed with a method of choice, e.g., Monte Carlo, probabilistic collocation method (PCM), multi-element probabilistic collocation method (ME-PCM).

A discrete analogue of a continuous random field  $\mathcal{M}(x; \omega)$  is denoted by a matrix  $\mathbf{M}_{\bar{\mathbf{x}}} \in \mathbb{R}^{\bar{n} \times n_s}$ . We define a column-wise inner product in the spatial domain between a matrix  $\mathbf{M}_{\bar{\mathbf{x}}}$  and a vector  $\mathbf{v}_{\bar{\mathbf{x}}} \in \mathbb{R}^{\bar{n}}$  as:

$$\mathbf{z} = \langle \mathbf{M}_{\bar{\mathbf{x}}}, \mathbf{v}_{\bar{\mathbf{x}}} \rangle_x = \mathbf{M}_{\bar{\mathbf{x}}}^T \mathbf{W}_{\bar{\mathbf{x}}} \mathbf{v}_{\bar{\mathbf{x}}}.$$

Here,  $\mathbf{z} \in \mathbb{R}^{n_s}$  is a vector, where each element of  $\mathbf{z}$  is the inner product of a column of  $\mathbf{M}_{\bar{\mathbf{x}}}$  and  $\mathbf{v}_{\bar{\mathbf{x}}}$ .  $\mathbf{W}_{\bar{\mathbf{x}}} = \text{diag}(\mathbf{w}_{\bar{\mathbf{x}}})$  denotes a diagonal matrix comprising of integration (e.g., quadrature) weights in the spatial domain. Similar to  $\mathbf{v}_{\bar{\mathbf{x}}}$ , the weights can be separated into two subsets,  $\mathbf{w}_{\bar{\mathbf{x}}} = [\mathbf{w}_{\mathbf{x}}; \mathbf{w}_{\mathbf{x}_b}]$  and  $\mathbf{W}_{\mathbf{x}} = \text{diag}(\mathbf{w}_{\mathbf{x}})$ ,  $\mathbf{W}_{\mathbf{x}_b} = \text{diag}(\mathbf{w}_{\mathbf{x}_b})$ . For example, if the spectral element method is used for discretization of the spatial domain, the weights would denote the quadrature weights. For the special case of  $n_s = 1$ , we retain the inner product of two vectors and the resultant value is a scalar. For two vectors,  $\mathbf{v}_{\bar{\mathbf{x}}}$  and  $\mathbf{u}_{\bar{\mathbf{x}}}$ , the above inner product converges to the inner product in the continuous form as the size of the discrete representation increases:

$$\lim_{\bar{n} \rightarrow \infty} \langle \mathbf{u}_{\bar{\mathbf{x}}}, \mathbf{v}_{\bar{\mathbf{x}}} \rangle_x = \int_D u(x)v(x)dx.$$

Similarly, we define the row-wise inner product between a matrix  $\mathbf{M}_{\bar{\mathbf{x}}} \in \mathbb{R}^{\bar{n} \times n_s}$  and a vector  $\mathbf{y} \in \mathbb{R}^{n_s}$  in the random space,

$$\mathbf{v}_{\bar{\mathbf{x}}} = \langle \mathbf{M}_{\bar{\mathbf{x}}}, \mathbf{y} \rangle_{\xi} = \mathbf{M}_{\bar{\mathbf{x}}} \mathbf{W}_{\xi} \mathbf{y},$$

where  $\mathbf{v}_{\bar{\mathbf{x}}} \in \mathbb{R}^{\bar{n}}$  is a vector and  $\mathbf{W}_{\xi} = \text{diag}(\mathbf{w}_{\xi})$  denotes a diagonal matrix comprising of weights of the discrete samples in the random space. Similar to the spatial representation, for the special case of  $\bar{n} = 1$ , we retain the inner product of two vectors in the random space and the resultant value will be a scalar. For two vectors  $\mathbf{y} \in \mathbb{R}^{n_s}$  and  $\mathbf{z} \in \mathbb{R}^{n_s}$ , the above equation converges to the correlation between two random variables as the number of samples increases:

$$\lim_{n_s \rightarrow \infty} \langle \mathbf{y}^T, \mathbf{z} \rangle_{\xi} = \int_{\Omega} y(\omega)z(\omega)\rho(\omega)d\omega,$$

where  $\rho(\omega)$  denotes the probability density function.

The SPDEs defined in Eq.(2.1-2.3) can be written in the discrete form in the spatial and random spaces as in the following:

$$(2.4) \quad \dot{\mathbf{V}}_{\mathbf{x}}(t) = \mathbf{N}_{\mathbf{x}}(t),$$

$$(2.5) \quad a\mathbf{V}_{\mathbf{x}_b}(t) + b\mathbf{D}_{\mathbf{x}_b, \bar{\mathbf{x}}} \mathbf{V}_{\bar{\mathbf{x}}}(t) = \mathbf{g}_{\mathbf{x}_b}(t),$$

$$(2.6) \quad \mathbf{V}_{\bar{\mathbf{x}}}(t_0) = \mathbf{V}_0.$$

In the above equation, the matrix  $\mathbf{N}_{\mathbf{x}}(t)$  is in general a nonlinear function of  $\mathbf{V}_{\mathbf{x}}(t)$ , i.e.,  $\mathbf{N}_{\mathbf{x}}(t) = \mathbf{N}_{\mathbf{x}}(\mathbf{V}_{\mathbf{x}}(t), t)$ . We also denote the discrete normal derivative operator by matrix  $\mathbf{D}_{\mathbf{x}_b, \bar{\mathbf{x}}} \in \mathbb{R}^{n_b \times \bar{n}}$ . In most discretization schemes,  $\mathbf{D}_{\mathbf{x}_b, \bar{\mathbf{x}}} \in \mathbb{R}^{n_b \times \bar{n}}$  is very sparse as mostly points nearby to the boundary have nonzero entries in the derivative matrix, e.g., spectral element and finite difference discretizations. Also,  $\mathbf{g}_{\mathbf{x}_b}(t) \in \mathbb{R}^{n_b}$  is a time-dependent vector. We also use the weighted Frobenius

norm of a matrix  $\mathbf{T} \in \mathbb{R}^{\bar{n} \times n_s}$  as in the following:

$$(2.7) \quad \|\mathbf{T}_{\bar{\mathbf{x}}}\|_F = \left( \sum_{i=1}^{\bar{n}} \sum_{j=1}^{n_s} w_{\bar{x}_i} w_{\xi_j} T_{\bar{\mathbf{x}}_{ij}}^2 \right)^{1/2}.$$

**2.2. Dynamically bi-orthonormal decomposition.** We use the dynamically bi-orthonormal decomposition defined in [1] to approximate a random field as it follows:

$$(2.8) \quad v(x, t; \omega) = \sum_{i=1}^r \sum_{j=1}^r u_i(x, t) \Sigma_{ij}(t) y_j(t; \omega) + e(x, t; \omega),$$

where  $u_i(x, t)$ ,  $i = 1, 2, \dots, r$  are a set of orthonormal spatial modes,  $y_j(t; \omega)$ ,  $j = 1, 2, \dots, r$  are the stochastic modes and  $\Sigma_{ij}(t)$  is the factorization of the correlation matrix. We note that in Eq.(2.8), the mean field is not subtracted as it was done in the original DBO formulation presented in [1] and as a result,  $\mathbb{E}[y_i(t; \omega)]$  is not equal to zero. This is done to simplify the derivation of the variational principle. However, the presented methodology can be applied to the original DBO formulation, where the evolution equation for the mean is explicitly derived in a straightforward manner.

We use the discrete form of the stochastic and spatial modes in the DBO formulation by defining a matrix  $\mathbf{U}_{\bar{\mathbf{x}}}(t) \in \mathbb{R}^{\bar{n} \times r}$  in the spatial domain comprising the time-dependent orthonormal spatial modes,

$$\mathbf{U}_{\bar{\mathbf{x}}}(t) = [\mathbf{u}_{\bar{\mathbf{x}}_1}(t) | \mathbf{u}_{\bar{\mathbf{x}}_2}(t) | \dots | \mathbf{u}_{\bar{\mathbf{x}}_r}(t)]_{\bar{n} \times r}.$$

Here,  $\mathbf{u}_{\bar{\mathbf{x}}_i}(t)$  denotes a vector of spatial modes. We also define the stochastic modes as a time-dependent matrix:

$$\mathbf{Y}(t) = [\mathbf{y}_1(t) | \mathbf{y}_2(t) | \dots | \mathbf{y}_r(t)]_{n_s \times r},$$

where  $\mathbf{Y}(t) \in \mathbb{R}^{n_s \times r}$  is a matrix comprising of the time-dependent orthonormal stochastic vectors in the random space, where  $n_s$  is the number of samples. The discrete analogue of the DBO formulation given by Eq. (2.8) is given by:

$$(2.9) \quad \mathbf{V}_{\bar{\mathbf{x}}}(t) = \mathbf{U}_{\bar{\mathbf{x}}}(t) \mathbf{\Sigma}(t) \mathbf{Y}(t)^T + \mathbf{E}_{\bar{\mathbf{x}}}(t).$$

**2.3. Variational principle.** To determine the boundary conditions for the spatial modes, the presented method is informed by the realization that the DBO evolution equations are the optimality conditions of a variational principle. An analogous variational principle was recently introduced in [44] for the reduced order modeling of deterministic reactive species transport equation. Our approach is to define a *unified* evolutionary differential operator that encompasses both the interior domain as well as the boundary as shown below:

$$\mathbf{M}_{\bar{\mathbf{x}}}(t) = [\mathbf{N}_{\mathbf{x}}(t); \mathbf{B}_{\mathbf{x}_b}(t)],$$

where,  $\mathbf{B}_{\mathbf{x}_b}(t) \in \mathbb{R}^{n_b \times n_s}$  is the boundary operator that is defined later in this section. Here,  $\mathbf{N}_{\mathbf{x}}(t) \in \mathbb{R}^{n \times n_s}$  is a discrete matrix representation of  $\mathcal{N}(u)$ , where  $n$  represents the interior points in the domain and  $\mathbf{B}_{\mathbf{x}_b}(t)$  is a discrete representation of  $\mathcal{B}(u)$ . The variational principle for the

stochastic DBO seeks to minimize the following functional:

$$(2.10) \quad \mathcal{F}(\dot{\mathbf{U}}_{\bar{\mathbf{x}}}(t), \dot{\Sigma}(t), \dot{\mathbf{Y}}(t)) = \left\| \frac{d}{dt}(\mathbf{u}_{\bar{\mathbf{x}}_i}(t) \Sigma_{ij}(t) \mathbf{y}_j^T(t)) - \mathbf{M}_{\bar{\mathbf{x}}}(t) \right\|_F^2,$$

subject to the orthonormality of the spatial and stochastic bases i.e.,  $\langle \mathbf{u}_{\bar{\mathbf{x}}_i}(t), \mathbf{u}_{\bar{\mathbf{x}}_j}(t) \rangle_x = \delta_{ij}$  and  $\langle \mathbf{y}_i^T(t), \mathbf{y}_j^T(t) \rangle_{\xi} = \delta_{ij}$ . Here,  $\mathbf{M}_{\bar{\mathbf{x}}}(t) \in \mathbb{R}^{\bar{n} \times n_s}$  is a matrix, representing  $\mathcal{M}(u)$  in the discrete form, where  $\bar{n}$  and  $n_s$  represent the number of discrete points in the spatial domain and the number of samples in the random space, respectively. In simple words, the variational principle seeks to minimize the distance between the time derivative of the DBO decomposition and the right hand of SPDE by optimally updating  $\mathbf{U}_{\bar{\mathbf{x}}}(t)$ ,  $\mathbf{Y}(t)$  and  $\Sigma(t)$ .

**2.4. Boundary condition for TDB.** We incorporate the boundary points by specifying the boundary evolution operator  $\mathbf{B}_{\mathbf{x}_b}(t)$  analogous to the way the interior points are treated in the variational principle, i.e., the boundary operator must prescribe the time derivative of the values at the boundary:  $\mathbf{B}_{\mathbf{x}_b}(t) = \dot{\mathbf{V}}_{\mathbf{x}_b}(t)$ . The variational principle then also accounts for the distance between the rate of change of DBO decomposition at the boundary points and  $\mathbf{B}_{\mathbf{x}_b}$ . To obtain  $\mathbf{B}_{\mathbf{x}_b}(t)$ , let the boundary condition be defined according to Eq.(2.5):

$$a\mathbf{V}_{\mathbf{x}_b}(t) + b\mathbf{D}_{\mathbf{x}_b, \mathbf{x}}(t)\mathbf{V}_{\bar{\mathbf{x}}}(t) = \mathbf{g}_{\mathbf{x}_b}(t).$$

Taking the time derivative of the above equation and after some simplifications, we obtain an expression for  $\dot{\mathbf{V}}_{\mathbf{x}_b}(t)$ . these steps are shown below:

$$\begin{aligned} a\dot{\mathbf{V}}_{\mathbf{x}_b}(t) + b\mathbf{D}_{\mathbf{x}_b, \bar{\mathbf{x}}}\dot{\mathbf{V}}_{\bar{\mathbf{x}}}(t) &= \dot{\mathbf{g}}_{\mathbf{x}_b}(t), \\ a\dot{\mathbf{V}}_{\mathbf{x}_b}(t) + b\mathbf{D}_{\mathbf{x}_b, \mathbf{x}_b}\dot{\mathbf{V}}_{\mathbf{x}_b}(t) + b\mathbf{D}_{\mathbf{x}_b, \mathbf{x}}\dot{\mathbf{V}}_{\mathbf{x}}(t) &= \dot{\mathbf{g}}_{\mathbf{x}_b}(t), \\ (a\mathbf{I} + b\mathbf{D}_{\mathbf{x}_b, \mathbf{x}_b})\dot{\mathbf{V}}_{\mathbf{x}_b}(t) &= \dot{\mathbf{g}}_{\mathbf{x}_b}(t) - b\mathbf{D}_{\mathbf{x}_b, \mathbf{x}}\dot{\mathbf{V}}_{\mathbf{x}}(t), \\ \dot{\mathbf{V}}_{\mathbf{x}_b}(t) &= (a\mathbf{I} + b\mathbf{D}_{\mathbf{x}_b, \mathbf{x}_b})^{-1} \left( \dot{\mathbf{g}}_{\mathbf{x}_b}(t) - b\mathbf{D}_{\mathbf{x}_b, \mathbf{x}}\dot{\mathbf{V}}_{\mathbf{x}}(t) \right). \end{aligned}$$

In the above derivation, we have used:  $\mathbf{D}_{\mathbf{x}_b, \bar{\mathbf{x}}}\dot{\mathbf{V}}_{\bar{\mathbf{x}}}(t) = \mathbf{D}_{\mathbf{x}_b, \mathbf{x}_b}\dot{\mathbf{V}}_{\mathbf{x}_b}(t) + \mathbf{D}_{\mathbf{x}_b, \mathbf{x}}\dot{\mathbf{V}}_{\mathbf{x}}(t)$  and  $\mathbf{I}$  is the identity matrix of size  $n_b \times n_b$ . The evolution of the points in the interior domain is given by  $\mathbf{N}_{\mathbf{x}}(t)$  and the evolution of points on the boundary is given by  $\mathbf{B}_{\mathbf{x}_b}(t)$ . Thus, the above equation can be written as:

$$(2.11) \quad \mathbf{B}_{\mathbf{x}_b}(t) = (a\mathbf{I} + b\mathbf{D}_{\mathbf{x}_b, \mathbf{x}_b})^{-1} (\dot{\mathbf{g}}_{\mathbf{x}_b}(t) - b\mathbf{D}_{\mathbf{x}_b, \mathbf{x}}\mathbf{N}_{\mathbf{x}}(t)).$$

We note that in the Eq. (2.11),  $a\mathbf{I} + b\mathbf{D}_{\mathbf{x}_b, \mathbf{x}_b}$  is a diagonal matrix, and therefore its inversion is not computationally costly.

**Theorem 2.1.** *Let Eq.(2.9) represent the DBO decomposition of the solution of SPDEs given in Eq.(2.4-2.6). Then the optimality conditions of the variational principle given by Eq.(2.10) are the*

following evolution equations for the DBO components:

$$(2.12) \quad \dot{\mathbf{u}}_{\mathbf{x}_i} = \left[ \langle \mathbf{N}_{\mathbf{x}}, \mathbf{y}_j \rangle_{\xi} - \mathbf{u}_{\mathbf{x}_k} \langle \mathbf{u}_{\bar{\mathbf{x}}_k}, \langle \mathbf{M}_{\bar{\mathbf{x}}}, \mathbf{y}_j \rangle_{\xi} \rangle_x \right] \Sigma_{ij}^{-1},$$

$$(2.13) \quad \dot{\mathbf{u}}_{\mathbf{x}_{b_i}} = \left[ \langle \mathbf{B}_{\mathbf{x}_b}, \mathbf{y}_j \rangle_{\xi} - \mathbf{u}_{\mathbf{x}_{b_k}} \langle \mathbf{u}_{\bar{\mathbf{x}}_k}, \langle \mathbf{M}_{\bar{\mathbf{x}}}, \mathbf{y}_j \rangle_{\xi} \rangle_x \right] \Sigma_{ij}^{-1},$$

$$(2.14) \quad \dot{\mathbf{y}}_i = \left[ \langle \mathbf{M}_{\bar{\mathbf{x}}}, \mathbf{u}_{\bar{\mathbf{x}}_j} \rangle_x - \mathbf{y}_k \langle \mathbf{y}_k^T, \langle \mathbf{M}_{\bar{\mathbf{x}}}, \mathbf{u}_{\bar{\mathbf{x}}_j} \rangle_x \rangle_{\xi} \right] \Sigma_{ji}^{-1},$$

$$(2.15) \quad \dot{\Sigma}_{ij} = \langle \langle \mathbf{u}_{\bar{\mathbf{x}}_i}, \mathbf{M}_{\bar{\mathbf{x}}} \rangle_x, \mathbf{y}_j \rangle_{\xi}.$$

In the above equations, explicit dependence to  $t$  is dropped for the sake of brevity. A similar proof for Theorem (2.1) is given in detail in Appendix A of [44] with two minor differences: (i) in [44], the coefficients  $\mathbf{y}$  are orthonormal with respect to the of inner product with an identity weight, i.e.,  $\mathbf{y}_i^T \mathbf{y}_j = \delta_{ij}$ , whereas in the present formulation, the  $\mathbf{y}$  coefficients are orthonormal with respect to the weighted inner product given by:  $\mathbf{y}_i^T \mathbf{W}_{\xi} \mathbf{y}_j = \delta_{ij}$ . (ii) In this paper, the variational principle is applied to the space-discretized form of the equations. Accounting for these two minor differences, according to [44], the optimality conditions lead to the closed-form evolution equation for the DBO components.

$$(2.16) \quad \dot{\mathbf{u}}_{\mathbf{x}_i} = \left[ \langle \mathbf{M}_{\bar{\mathbf{x}}}, \mathbf{y}_j \rangle_{\xi} - \mathbf{u}_{\mathbf{x}_k} \langle \mathbf{u}_{\bar{\mathbf{x}}_k}, \langle \mathbf{M}_{\bar{\mathbf{x}}}, \mathbf{y}_j \rangle_{\xi} \rangle_x \right] \Sigma_{ij}^{-1} + \mathbf{u}_{\mathbf{x}_j} \varphi_{ji},$$

$$(2.17) \quad \dot{\mathbf{y}}_i = \left[ \langle \mathbf{M}_{\bar{\mathbf{x}}}, \mathbf{u}_{\bar{\mathbf{x}}_j} \rangle_x - \mathbf{y}_k \langle \mathbf{y}_k^T, \langle \mathbf{M}_{\bar{\mathbf{x}}}, \mathbf{u}_{\bar{\mathbf{x}}_j} \rangle_x \rangle_{\xi} \right] \Sigma_{ji}^{-1} + \mathbf{y}_j \theta_{ji},$$

$$(2.18) \quad \dot{\Sigma}_{ij} = \langle \langle \mathbf{u}_{\bar{\mathbf{x}}_i}, \mathbf{M}_{\bar{\mathbf{x}}} \rangle_x, \mathbf{y}_j \rangle_{\xi} - \varphi_{ik} \Sigma_{kj} - \Sigma_{ik} \theta_{kj}.$$

It was also shown in [44] that any skew-symmetric choice for matrices  $\varphi_{ij}$  and  $\theta_{ij}$  leads to equivalent low-rank approximations, i.e., the subspaces spanned by  $\mathbf{u}_{\mathbf{x}_i}$  and  $\mathbf{y}_i$  modes are identical for any skew-symmetric  $\varphi_{ij}$  and  $\theta_{ij}$ . We choose the simplest form, i.e., dynamically orthogonal condition, i.e.,  $\varphi_{ij} = 0$  and  $\theta_{ij} = 0$ . Replacing  $\mathbf{M}_{\bar{\mathbf{x}}} = [\mathbf{N}_{\mathbf{x}}; \mathbf{B}_{\mathbf{x}_b}]$  in Eqs.(2.16-2.18) and using  $\varphi_{ij} = 0$  and  $\theta_{ij} = 0$  result in Eqs.(2.12-2.15).

Eq.(2.13) describes the evolution of the value of the spatial modes at the boundary. Substituting the value of  $\mathbf{B}_{\mathbf{x}_b}(t)$  from Eq.(2.11) in Eq.(2.13), we obtain the evolution of the spatial modes at the boundary,

$$(2.19) \quad \dot{\mathbf{u}}_{\mathbf{x}_{b_i}} = \left[ \langle (a\mathbf{I} + b\mathbf{D}_{\mathbf{x}_b, \mathbf{x}_b})^{-1} (\dot{\mathbf{g}}_{\mathbf{x}_b} - b\mathbf{D}_{\mathbf{x}_b, \mathbf{x}} \mathbf{N}_{\mathbf{x}}), \mathbf{y}_j \rangle_{\xi} - \mathbf{u}_{\mathbf{x}_{b_k}} \langle \mathbf{u}_{\bar{\mathbf{x}}_k}, \langle \mathbf{M}_{\bar{\mathbf{x}}}, \mathbf{y}_j \rangle_{\xi} \rangle_x \right] \Sigma_{ij}^{-1}.$$

The above equation the evolution of the spatial modes at the boundary for Dirichlet, Neumann and Robin, which can be specified for different choices of  $a$  and  $b$ .

**Remark 2.2.** Eq.(2.13) determines the evolution of the spatial modes at the boundaries. It also reveals how the values of the modes at the boundary are coupled to the state of the modes globally due to the appearance of the term  $\langle \mathbf{u}_{\bar{\mathbf{x}}_k}(t), \langle \mathbf{M}_{\bar{\mathbf{x}}}(t), \mathbf{y}_j(t) \rangle_{\xi} \rangle_x$ , which utilizes the values of the spatial modes as well as  $\mathbf{M}_{\bar{\mathbf{x}}}(t)$  at every discrete point ( $\bar{\mathbf{x}}$ ). It is also straightforward to show that Eq.(2.12) and Eq.(2.13) together satisfy the dynamically orthogonal condition ( $\langle \dot{\mathbf{u}}_{\bar{\mathbf{x}}_i}(t), \mathbf{u}_{\bar{\mathbf{x}}_j}(t) \rangle_x = 0$ ), and therefore, the spatial modes remain orthonormal in the discrete sense. This means that specifying the boundary conditions according to Eq.(2.13), preserves the orthonormality constraints of the DBO spatial modes.

**Remark 2.3.** In the discrete representation, non-homogeneous boundary conditions appear as a source term for the evolution equations of  $\mathbf{y}_i$  and  $\Sigma_{ij}$ . This can be realized by observing that in



the right hand side of Eq.(2.14) and Eq.(2.15):

$$(2.20) \quad \langle \mathbf{M}_{\bar{\mathbf{x}}}(t), \mathbf{u}_{\bar{\mathbf{x}}_j}(t) \rangle_x = \mathbf{N}_{\mathbf{x}}(t) \mathbf{W}_x \mathbf{u}_{\mathbf{x}_j}(t) + \mathbf{B}_{\mathbf{x}_b}(t) \mathbf{W}_{\mathbf{x}_b} \mathbf{u}_{\mathbf{x}_{b_j}}(t).$$

The second term in the above equation is the contribution of the boundary condition that appears in the right-hand side of the evolution equations of  $\mathbf{y}_i$  and  $\Sigma_{ij}$ . In the continuous limit, the contribution of the boundary terms to  $\mathbf{y}_i$  and  $\Sigma_{ij}$  is zero as the boundary points are of measure zero in comparison to the contribution of the interior points. However, in the discrete representation, these terms are nonzero.

*Remark 2.4.* Although the evolution equations in Theorem 2.1 have been derived without subtracting the mean from the stochastic field, the variational principle can be easily extended to the mean subtracted form of equations.

**2.5. Dynamically orthogonal decomposition.** The extension of the above procedure to the DO formulation is straightforward. The discrete analogue of the DBO formulation given by Eq. (2.8) is given by:

$$(2.21) \quad \mathbf{V}_{\bar{\mathbf{x}}}(t) = \mathbf{U}_{\bar{\mathbf{x}}}(t) \mathbf{Y}(t)^T + \mathbf{E}_{\bar{\mathbf{x}}}(t).$$

where  $\mathbf{U}_{\bar{\mathbf{x}}}(t) \in \mathbb{R}^{\bar{n} \times r}$  is the matrix of time-dependent orthonormal spatial modes and  $\mathbf{Y}(t) \in \mathbb{R}^{n_s \times r}$ . See [2] for more details. The corresponding variational principle for the DO decomposition is given by:

$$\mathcal{F}(\dot{\mathbf{U}}_{\bar{\mathbf{x}}}(t), \dot{\mathbf{Y}}(t)) = \left\| \frac{d}{dt} (\mathbf{u}_{\bar{\mathbf{x}}_i}(t) \mathbf{y}_i^T(t)) - \mathbf{M}_{\bar{\mathbf{x}}}(t) \right\|_F^2,$$

subject to the orthonormality of the spatial modes. The optimality conditions of the above variational principle leads to the closed-form evolution of  $\mathbf{U}_{\bar{\mathbf{x}}}(t)$  and  $\mathbf{Y}(t)$ . For more details see [36]. This leads to the following equations for evolution of spatial and stochastic modes:

$$(2.22) \quad \dot{\mathbf{u}}_{\mathbf{x}_i} = \left[ \langle \mathbf{N}_{\mathbf{x}}, \mathbf{y}_j \rangle_{\xi} - \mathbf{u}_{\mathbf{x}_k} \langle \mathbf{u}_{\bar{\mathbf{x}}_k}, \langle \mathbf{M}_{\bar{\mathbf{x}}}, \mathbf{y}_j \rangle_{\xi} \rangle_x \right] C_{ij}^{-1},$$

$$(2.23) \quad \dot{\mathbf{u}}_{\mathbf{x}_{b_i}} = \left[ \langle \mathbf{B}_{\mathbf{x}_b}, \mathbf{y}_j \rangle_{\xi} - \mathbf{u}_{\mathbf{x}_{b_k}} \langle \mathbf{u}_{\bar{\mathbf{x}}_k}, \langle \mathbf{M}_{\bar{\mathbf{x}}}, \mathbf{y}_j \rangle_{\xi} \rangle_x \right] C_{ij}^{-1},$$

$$(2.24) \quad \dot{\mathbf{y}}_i = \langle \mathbf{M}_{\bar{\mathbf{x}}}, \mathbf{u}_{\bar{\mathbf{x}}_i} \rangle_x.$$

In the above equations, the dependence of the matrices on  $t$  is dropped for the sake of brevity. Remarks 2.2-2.4 are applicable to the above DO formulation with the only difference that the matrix  $\Sigma(t)$  in the DBO formulation is absorbed to  $\mathbf{Y}(t)$  coefficient in the DO formulation.

**2.6. Validation against the optimal decomposition.** We will evaluate the performance of the presented methodology against the optimal low-rank approximation obtained by performing Karhunen-Lo  ve (KL) decomposition. The KL decomposition for a random field  $v(x, t; \omega)$  is given by:

$$v(x, t; \omega) = \sum_{i=1}^{\infty} \sqrt{\lambda_i(t)} u_i^{KL}(x, t) y_i^{KL}(t; \omega), \quad x \in \bar{D},$$

where  $\lambda_i(t)$  represents the eigenvalues of the correlation operator and  $u_i^{KL}(x, t)$  are the eigenfunctions of the covariance kernel and  $y_i^{KL}(t; \omega)$  are mutually uncorrelated random variables given by,

$$y_i^{KL}(t; \omega) = \frac{1}{\sqrt{\lambda_i(t)}} \int_D v(x, t; \omega) u_i^{KL}(x, t) dx.$$

The eigenfunctions  $u_i^{KL}(x, t)$  are orthonormal and the stochastic processes  $y_i^{KL}(t; \omega)$  are uncorrelated, i.e.:  $\mathbb{E}[y_i^{KL} y_j^{KL}] = \delta_{ij}$ . The KL decomposition gives the best representation of a stochastic field in terms of the mean-squared error. In the discrete form, the KL decomposition is obtained by taking the instantaneous singular value decomposition (SVD) of the matrix of samples obtained using the probabilistic collocation method using the appropriate inner product in the spatial and random spaces as described in Section 2.1. To assess the performance of the presented methodology, we compare the singular values obtained from the DBO and DO decompositions against those corresponding components obtained from the KL decomposition. For the comparison of DO and DBO modes versus the KL decomposition, the spatial modes in DO and DBO must be energetically ranked via an in-subspace rotation as explained in [1]. Since the truncated KL decomposition provides the best instantaneous low-rank approximation, it is used to validate the results obtained from DBO and DO in the subsequent sections. In particular, since the KL decomposition is performed over the entire domain, i.e, including the boundary points, the value of the KL modes at the boundary is compared against the presented methodology.

### 3. Demonstration cases.

**3.1. Linear advection-diffusion equation.** As the first demonstration, we consider a linear advection-diffusion equation governed by:

$$(3.1) \quad \frac{\partial u}{\partial t} + c \frac{\partial u}{\partial x} = \nu \frac{\partial^2 u}{\partial x^2}, \quad x \in [0, 5] \text{ and } t \in [0, t_f],$$

$$(3.2) \quad u(x, 0; \omega) = \cos(2\pi x) + \sigma_x \sum_{i=1}^d \sqrt{\lambda_{x_i}} u_i(x) \xi_i(\omega), \quad x \in [0, 5], \xi_i \sim \mathcal{U}[-1, 1],$$

$$(3.3) \quad au + b \frac{\partial u}{\partial x} = g(x, t, \omega), \quad x = 0,$$

$$(3.4) \quad \frac{\partial u}{\partial x} = 0, \quad x = 5.$$

Here,  $\nu$  is taken to be 0.05 and  $c = 1$ . Homogeneous Neumann boundary condition is imposed at  $x = 5$  for all the cases considered below. The randomness in the system comes from the stochastic left boundary ( $x = 0$ ) and random initial conditions. We consider three types of stochastic boundary conditions at  $x = 0$ : (i) Dirichlet, ( $b = 0, a \neq 0$ ) (ii) Neumann ( $a = 0, b \neq 0$ ), and (iii) Robin ( $a \neq 0, b \neq 0$ ). The results for these cases are presented in the subsequent sections. The SPDE given by Eq.(3.1-3.4) is solved using two methods: (i) DBO method according to Eq.(2.12-2.15), (ii) DO method according to Eq.(2.22-2.24). For spatial discretization of the domain, the spectral/hp element method is used with  $N_e = 101$  and polynomial order 4 which results in the total number of points in the physical space to be  $\bar{n} = 405$ . Uniform distribution is taken in all directions of the random space. The random space is discretized using sparse grid to get the quadrature weights and coordinates for the sample points [10, 13]. The random space dimension is chosen based on the 99.99% energy of the covariance kernel, which resulted in  $d = 8$ . For the sparse grid, we use level 3, which results in the total sample size of  $n_s = 333$ . The fourth-order Runge-Kutta method is

used for time integration with  $\Delta t = 5 \times 10^{-4}$ . The system is evolved till  $t_f = 5$ . These parameters, namely the spatial discretization, random samples, and  $\Delta t$  remain unchanged for all the three cases of boundaries in the linear advection-diffusion equation. The DBO and DO solutions are compared with the PCM solution and the global error between the two fields is defined as,

$$(3.5) \quad \mathbf{E}_g(\bar{\mathbf{x}}, t) = \mathbf{V}_{DBO}(\bar{\mathbf{x}}, t) - \mathbf{V}_{PCM}(\bar{\mathbf{x}}, t),$$

$$(3.6) \quad \mathcal{E}_g(t) = \|\mathbf{E}_g(\bar{\mathbf{x}}, t)\|_F.$$

Similarly, the error at the boundary for Dirichlet and Robin boundary conditions ( $a \neq 0$ ) is computed according to:

$$(3.7) \quad \mathbf{E}_b(\mathbf{x}_b, t) = \mathbf{V}_{DBO}(\mathbf{x}_b, t) - \frac{1}{a} (\mathbf{g}_{\mathbf{x}_b}(t) - b \mathbf{D}_{\mathbf{x}_b, \bar{\mathbf{x}}} \mathbf{V}_{\bar{\mathbf{x}}}(t)),$$

$$(3.8) \quad \mathcal{E}_b(t) = \left( \sum_{i=1}^{n_b} \sum_{j=1}^{n_s} w_{x_{b_i}} w_{\xi_j} E_{b_{ij}}^2 \right)^{1/2}.$$

The boundary error for Neumann boundary ( $a = 0, b \neq 0$ ) is computed as,

$$(3.9) \quad \mathbf{E}_b(\mathbf{x}_b, t) = \mathbf{D}_{\mathbf{x}_b, \bar{\mathbf{x}}} \mathbf{V}_{DBO}(\bar{\mathbf{x}}, t) - \frac{1}{b} (\mathbf{g}_{\mathbf{x}_b}(t)),$$

$$(3.10) \quad \mathcal{E}_b(t) = \left( \sum_{i=1}^{n_b} \sum_{j=1}^{n_s} w_{x_{b_i}} w_{\xi_j} E_{b_{ij}}^2 \right)^{1/2}.$$

We also evaluate the performance of the presented method against instantaneous Karhunen Loéve (KL) decomposition, which is the best time-dependent subspaces in the  $L_2$  sense, which in the discrete form is described by the Frobenius norm. In particular, we compare the values of the KL modes at the boundary against the values obtained from the presented method.

**3.1.1. Stochastic Dirichlet boundary condition.** Dirichlet boundary condition is imposed at  $x = 0$  according to:

$$u(0, t; \omega) = g(t; \omega),$$

where  $g(t; \omega)$  is assumed to be a random process with a squared-exponential temporal kernel given by:

$$K(t, t') = \exp\left(\frac{-(t - t')^2}{2l_t^2}\right),$$

where,  $l_t$  is the temporal correlation length, which is taken to be 1.0. The eigen-decomposition of the above kernel results in:

$$\int_0^{t_f} K(t, t') \varphi_i(t') dt' = \lambda_{t_i} \varphi_i(t),$$

where  $\varphi_i(t)$  and  $\lambda_{t_i}$  are the eigenfunctions and eigenvalues of the temporal kernel respectively. The boundary condition is approximated with a truncated Karhunen-Loéve decomposition as given in

the following equation:

$$g(t; \omega) = 0.5 \cos(2\pi t) + \sigma_t \sum_{i=1}^d \sqrt{\lambda_{t_i}} \varphi_i(t) \xi_i(\omega).$$

Here,  $\xi(\omega)$  is discretized in a  $d$ -dimensional random space obtained by using ME-PCM sparse grid construction which gives  $\xi \in \mathbb{R}^{n_s \times d}$ . For this case,  $d = 8$  is taken as this approximation captures 99.99% of the random process.  $\sigma_t$  is taken to be 1.0. Similarly, to initialize the stochastic initial conditions, we take a squared-exponential kernel in the spatial domain,

$$K(x, x') = \exp\left(\frac{-(x - x')^2}{2l_x^2}\right),$$

where,  $l_x$  is the spatial correlation length which is taken to be 1.0. The eigen-decomposition of the kernel results in:

$$\int_{x_l}^{x_r} K(x, x') \psi_i(x') dx' = \lambda_{x_i} \psi_i(x),$$

where  $\psi_i(t)$  and  $\lambda_{x_i}$  are the eigenfunctions and eigenvalues of the spatial kernel and  $x_l = 0, x_r = 5$  are the left and right boundaries of the spatial domain respectively. The initial conditions are taken to be,

$$u(x, 0; \omega) = 0.5 \cos(2\pi x) + \sigma_x \sum_{i=1}^d \sqrt{\lambda_{x_i}} \psi_i(x) \xi_i(\omega).$$

Here,  $\xi_i \in \mathbb{R}^{n_s \times d}$  are the same discrete samples used in the time kernel. We take  $\sigma_x = 1.0$ . The system is numerically evolved till  $t_f = 5$  using the two methods: (i) DBO, (ii) DO. The obtained results are compared with the instantaneous KL decomposition and presented in Fig.(1-2). The first row of Fig.(1) shows the comparison of singular values for three different orders of model reduction,  $r = 5, 7$  & 9 for DBO, DO and KL. We observe that the singular values improve in comparison as the order of model reduction is improved. The second row shows the comparison of the value of different modes at the stochastic Dirichlet boundary at  $x = 0$ . The solution is exactly represented by  $r = 9$ . Hence, for the lower model reduction orders i.e.,  $r = 5$  and 7, the last mode of DBO and DO solution shows noticeable differences from the KL both in the singular values and the evolution of the modes at the boundary. The error in the solution for  $r = 5, 7$  can be attributed to the unresolved modes. The error comparison for the two methods as compared to KL is shown in Fig.(2). The global error in the representation of the solution i.e.,  $\mathcal{E}_g$ , evaluated according to Eq.(3.6), is shown in Fig.(2a). The error at the stochastic boundary i.e.,  $\mathcal{E}_b$ , evaluated by Eq.(3.8), is shown in Fig.(2b). For  $r = 9$ , when the solution is represented exactly, DBO and DO show the lowest errors of all model reduction order. However, between DBO and DO, DBO shows the highest accuracy for  $r = 9$  whereas the DO error for the same reduction order is a few orders of magnitude higher than the DBO error. The DBO boundary error for  $r = 9$  shows the same value as the KL error. We observe high error in DO for  $r = 9$  despite the seemingly equal singular value comparison. The source of the error can be traced back to the error in the singular values as shown in the Fig.(2c). The errors in third, sixth and ninth singular values for the case  $r = 9$  are shown. The  $L_2$ -errors are computed by comparing the DBO and DO singular values with

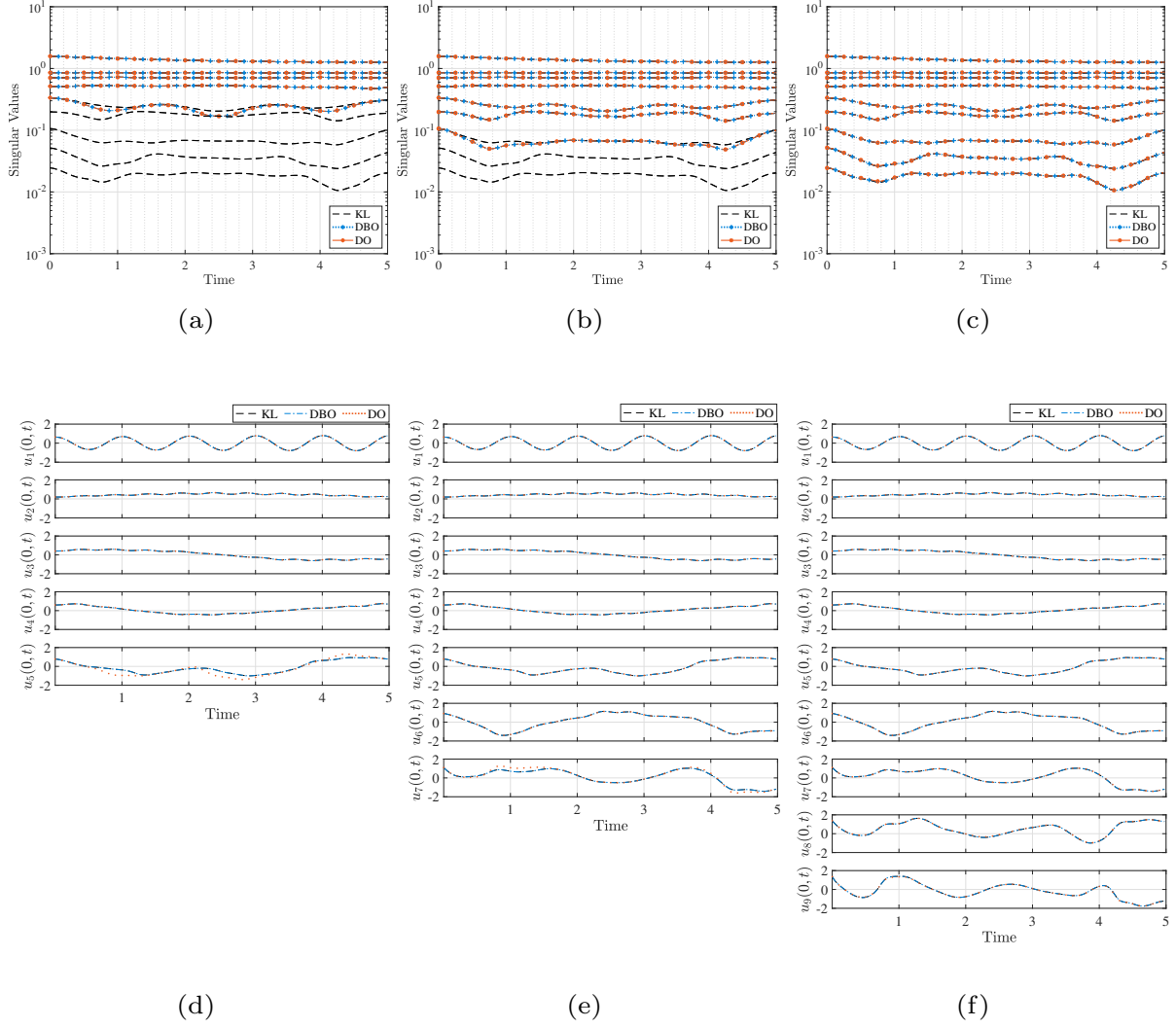


Figure 1: Linear advection-diffusion equation (i) Dirichlet boundary condition: The first row shows the singular value comparison for KL, DBO and DO methods. The values are compared for three model reduction orders,  $r = 5, 7$  &  $9$ . The evolution of the values of the modes at the stochastic left boundary are compared in the second row for the three aforementioned methods.

KL values. We observe that the DO solution shows significant deviation from the KL for  $r = 9$ , while DBO does not. This can be attributed to the better condition number for matrix inversion in DBO leading to lower errors [1]. The DO method has a condition number  $\lambda_{max}/\lambda_{min}$  (where  $\lambda_{min}$  and  $\lambda_{max}$  represent the smallest and largest eigenvalues of the covariance matrix), whereas the DBO method has a condition number  $\sqrt{\lambda_{max}/\lambda_{min}}$  since the factorization of the correlation matrix i.e.,  $\Sigma$  is inverted.



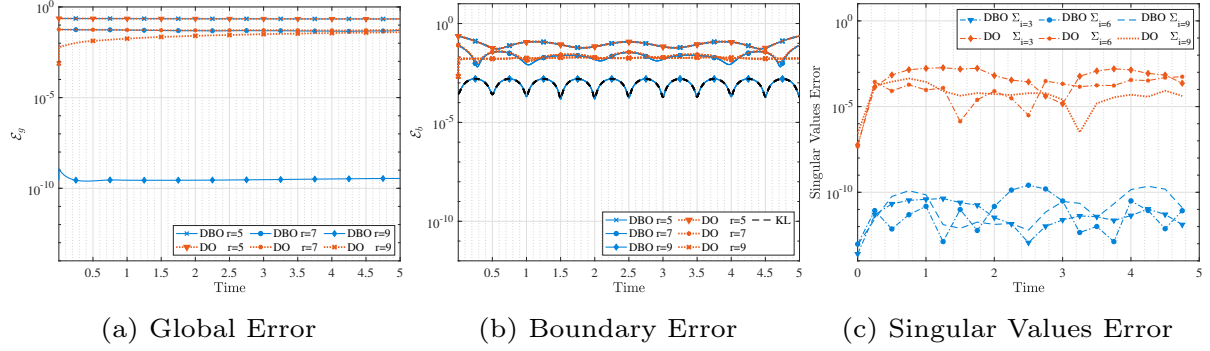


Figure 2: Linear advection-diffusion equation (i) Dirichlet boundary condition: The global and boundary error comparison is shown in (a) and (b) respectively. The lowest error is obtained using DBO method for  $r = 9$ . The singular values obtained from DO method for  $r = 9$  are riddled with errors. The  $L_2$ -error for the third, sixth and ninth singular values is compared in (c) for DO and DBO.

**3.1.2. Stochastic Neumann boundary condition.** The stochastic Neumann boundary condition is imposed on the left boundary,  $x = 0$  as,

$$b \frac{\partial u(0, t; \omega)}{\partial x} = g(t; \omega), \quad a = 0, b \neq 0.$$

For this case,  $b = 1$ . Similar to the problem setup as the Dirichlet boundary case, the function  $g(t; \omega)$  is taken as a function of eigenvectors and singular values of the squared exponential kernel and the initial conditions are taken as a function of eigenvectors and singular values of the spatial squared exponential kernel. The temporal correlation length,  $l_t$  is taken to be 1.0 and the spatial correlation length  $l_x$  is taken to be 1.0. The boundary conditions are taken to be,

$$g(t; \omega) = 2\pi \sin(2\pi t) + \sigma_t \sum_{i=1}^d \sqrt{\lambda_{t_i}} \varphi_i(t) \xi_i(\omega),$$

and the initial conditions are taken to be,

$$u(x, 0; \omega) = \cos(2\pi x) + \sigma_x \sum_{i=1}^d \sqrt{\lambda_{x_i}} \psi_i(x) \xi_i(\omega).$$

Here,  $\sigma_t = 0.1$  and  $\sigma_x = 0.5$ . The samples  $\xi \in \mathbb{R}^{n_s \times d}$  are same as the previous case. The results for these two methods are compared in Fig.(3-4) against the KL decomposition. The first row in Fig.(3), shows comparison between singular values for model reduction orders,  $r = 5, 7$  & 9. The singular values improve in comparison as the model reduction order is improved. The second row shows the comparison of the value of modes at the stochastic Neumann boundary at  $x = 0$ . Fig.(4a-b) show the global error comparison evaluated by Eq.(3.6), and boundary error comparison evaluated by Eq.(3.10) for the three reduction orders. Similar to the previous case, when the solution is exactly represented by  $r = 9$ , DBO and DO show the lowest errors of all reduction orders. Between DBO and DO, DBO shows higher accuracy for  $r = 9$ . This can be seen in the errors for  $r = 9$  for DBO

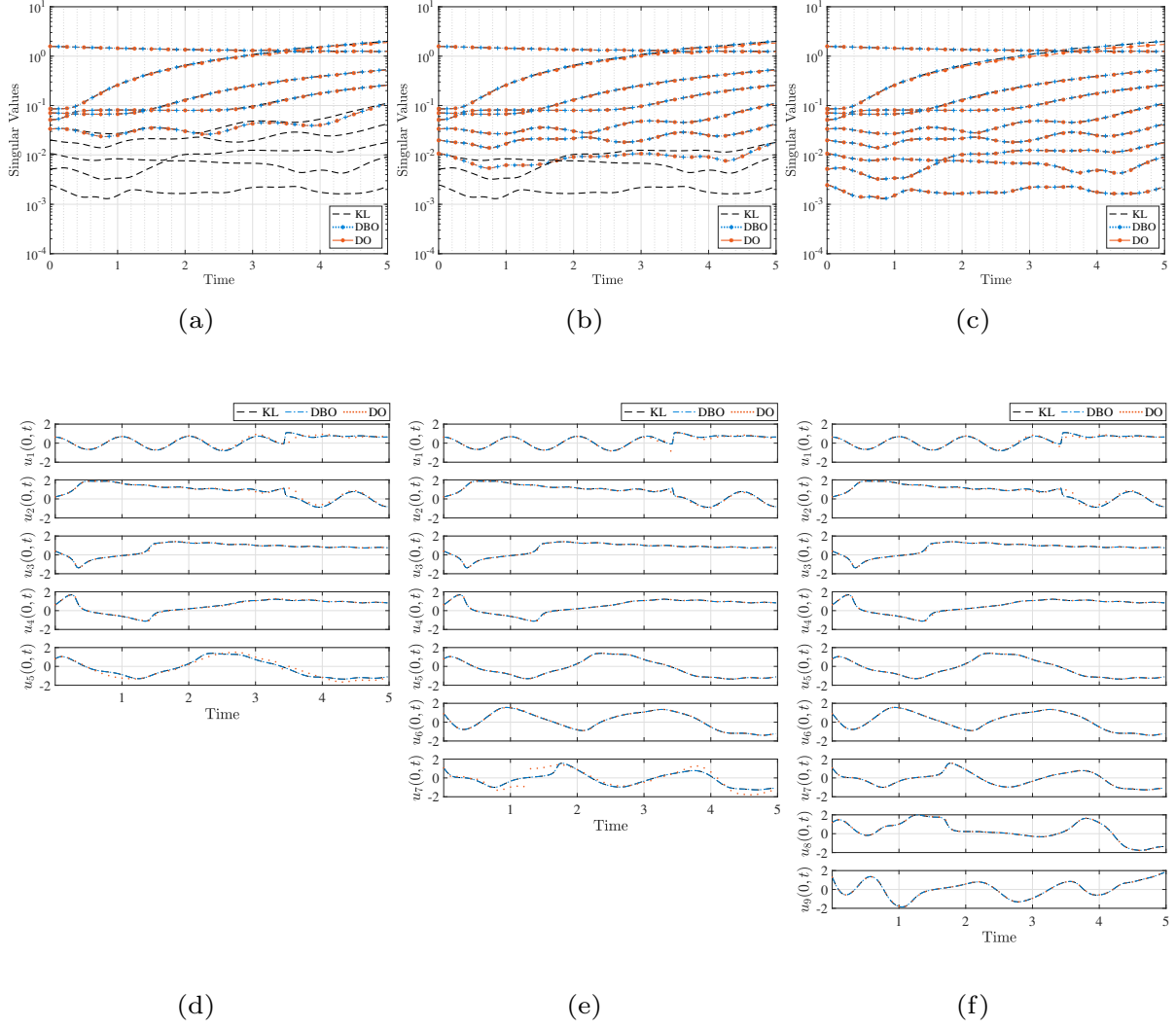


Figure 3: Linear advection-diffusion equation (ii) Neumann boundary condition: The first row shows the singular value comparison for KL, DBO and DO methods, The values are compared for three reduction orders,  $r = 5, 7$  and  $9$ . The evolution of the values of the modes at the left stochastic boundary are compared in the second row for the DO and DBO against KL.

and DO in Fig.(4a-b). DBO boundary error for  $r = 9$  shows the same value as the KL error. The error comparison between individual singular values is shown in Fig.(4c) for third, sixth and ninth singular values. This error in the DO solution causes the global and boundary error for  $r = 9$  to be higher than that of DBO error. This lower error for DBO method can be attributed to the fact that the DBO method has a better condition number for inversion of  $\Sigma$  matrix than DO method, which requires the inversion of the correlation matrix.

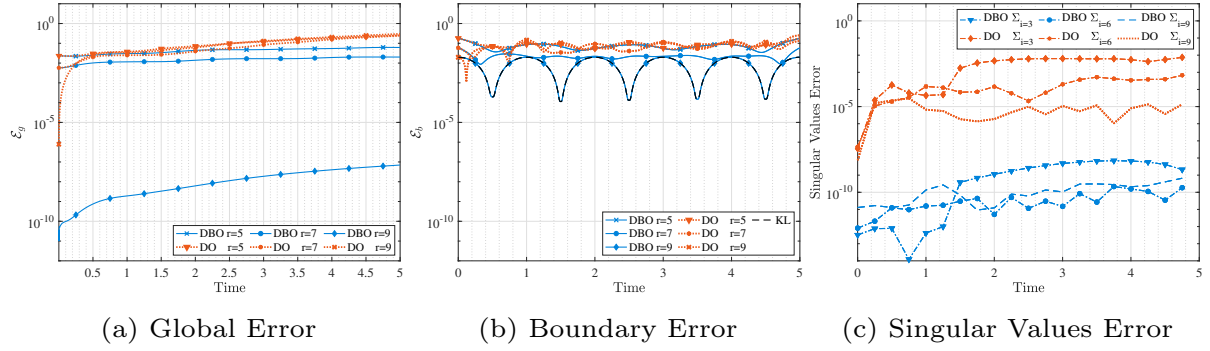


Figure 4: Linear advection-diffusion equation (ii) Neumann boundary condition: Error comparison for DBO and DO as compared with the KL solution. The global error,  $\mathcal{E}_g$  and the boundary error,  $\mathcal{E}_b$  are shown in (a) and (b) respectively. The lowest error is obtained using DBO method for  $r = 9$ . The  $L_2$ -error in the third, sixth and ninth singular value is compared in (c) for DO and DBO.

**3.1.3. Stochastic Robin boundary condition.** The stochastic Robin boundary condition is imposed on the left boundary at  $x = 0$  as,

$$au(0, t; \omega) + b \frac{\partial u(0, t; \omega)}{\partial x} = g(t; \omega), \quad a \neq 0, b \neq 0.$$

Similar to the problem setup as the previous cases, the function  $g(t; \omega)$  is taken as a function of eigenvectors and singular values of the squared exponential kernel and  $a = 0.1, b = 1$ . The temporal correlation length,  $l_t$  is taken to be 1 and the spatial correlation length  $l_x$  is taken to be 1. The boundary conditions are taken to be,

$$g(t; \omega) = -\cos(2\pi t) + 2\pi \sin(2\pi t) + \sigma_t \sum_{i=1}^d \sqrt{\lambda_{t_i}} \varphi_i(t) \xi_i(\omega),$$

and the initial conditions are taken to be,

$$u(x, 0; \omega) = \cos(2\pi x) + \sigma_x \sum_{i=1}^d \sqrt{\lambda_{x_i}} \psi_i(x) \xi_i(\omega).$$

Similar to the Dirichlet and Neumann boundary case,  $\xi_i(\omega)$  are discretized in 8-dimensional ( $d = 8$ ) random space using sparse grid. The samples are drawn from a uniform distribution. Here,  $\sigma_t = -0.1$  and  $\sigma_x = 0.01$ . The singular value evolution, evolution of modes at the boundary and error comparison for this case are shown in Fig.(5-6). The first row in Fig.(5), shows comparison between singular values for the model reduction orders,  $r = 5, 7$  &  $9$ . The singular values improve in comparison as the model reduction order is improved. The second row, shows the comparison of the modes at the stochastic boundary  $x = 0$ . Fig.(6a-b) show the global error comparison evaluated by Eq.(3.6) and boundary error comparison evaluated by Eq.(3.8) for the three reduction orders. Similar to the previous case, when the solution is exactly represented by  $r = 9$  for DBO and DO, show the lowest errors of all reduction orders. Between DBO and DO, DBO shows higher accuracy for  $r = 9$ . This can be seen in the errors for  $r = 9$  for DBO and DO in Fig.(6a-b). The boundary

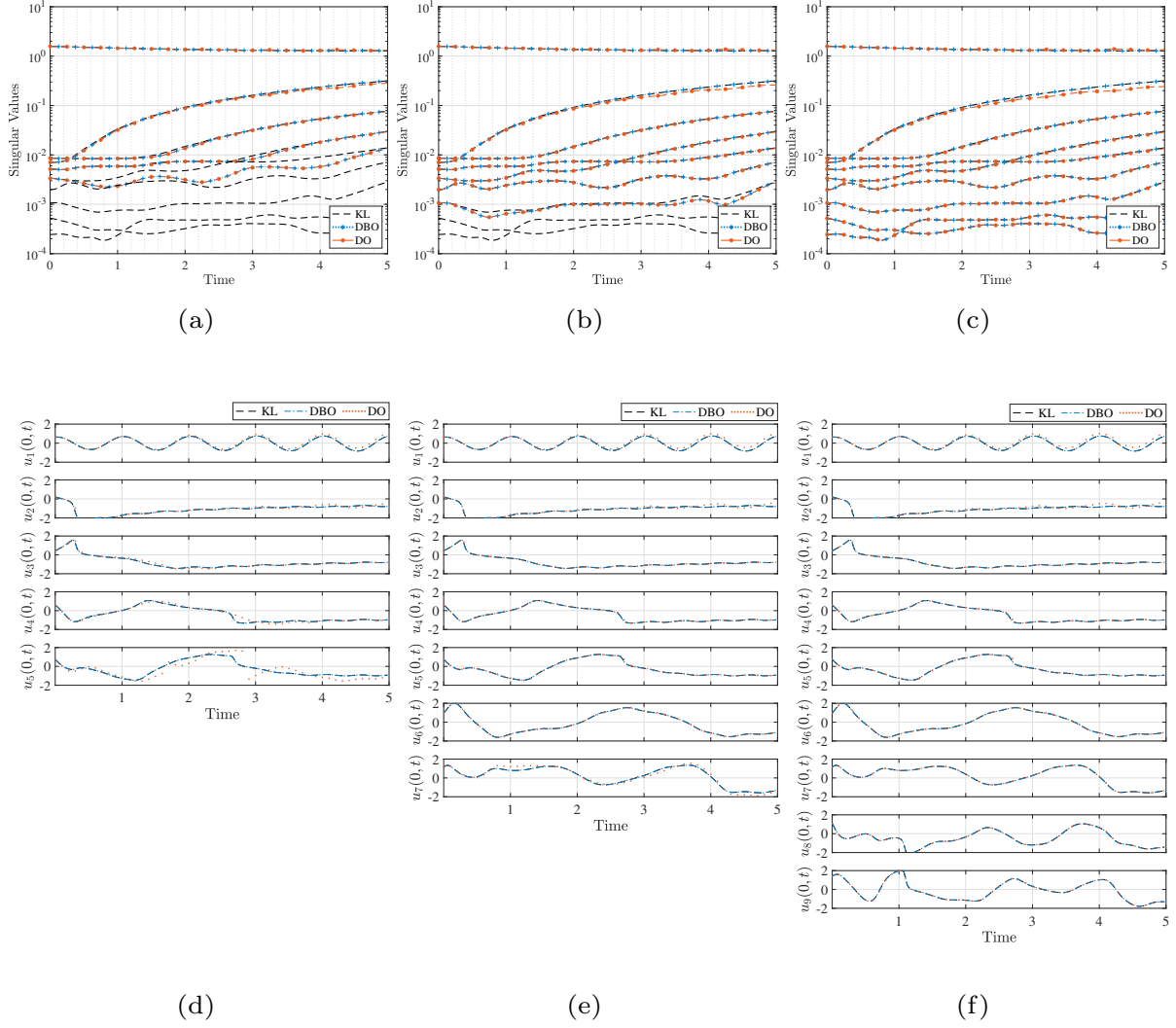


Figure 5: Linear advection-diffusion equation (iii) Robin boundary condition: The first row shows the singular value comparison for KL, DBO and DO methods. The values are compared for three reduction orders,  $r = 5, 7$  &  $9$ . The evolution of the values of the modes at the left stochastic boundary are compared in the second row for DO and DBO against KL.

error for  $r = 9$  for DBO shows the same error as the KL. The error comparison between individual singular values is shown in Fig.(6c) for third, sixth and ninth singular values for the case  $r = 9$ . This error in the individual singular values in the DO solution causes the global and boundary error for  $r = 9$  to be higher than that of DBO error.

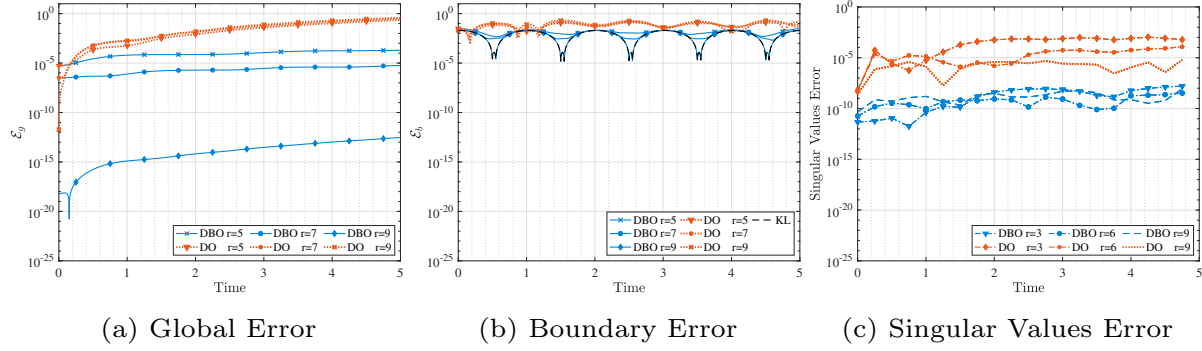


Figure 6: Linear advection-diffusion equation (iii) Robin boundary condition: Error comparison for DBO and DO as compared with the KL solution. The global and boundary error comparison are shown in (a) and (b) respectively. Lowest error is obtained using DBO method for  $r = 9$ .  $L_2$ -error in the third, sixth and ninth singular value is compared in (c) for DO and DBO.

**3.2. Burgers' equation.** As a demonstration for the nonlinear one-dimensional equation, we consider the Burgers' equation governed by:

$$(3.11) \quad \frac{\partial u}{\partial t} + u \frac{\partial u}{\partial x} = \nu \frac{\partial^2 u}{\partial x^2}, \quad x \in [0, 1] \text{ and } t \in [0, t_f],$$

$$(3.12) \quad u(x, 0; \omega) = \sin(2\pi x) + \sigma_x \sum_{i=1}^d \sqrt{\lambda_{x_i}} \psi_i(x) \xi_i(\omega), \quad x \in [0, 1],$$

with Dirichlet boundary condition at  $x = 0$  and homogeneous Neumann boundary condition at  $x = 1$ .  $\xi(\omega) \in \mathbb{R}^{n_s \times d}$  are the discrete points in  $d$ -dimensional random space obtained by using ME-PCM.  $\nu$  is taken to be 0.05. The random space is taken to be  $d = 4$  dimensional since it contains 99.99% of the energy in the covariance kernel and  $\sigma_x = 0.005$ . The 4-dimensional random space is discretized with the PCM tensor product rule [12, 50] with 4 quadrature points in each random direction which give the total samples to be  $n_s = 4^4 = 256$ .  $\lambda_{x_i}$  and  $\psi_i(x)$  are the eigenvalues and eigenvectors of the spatial squared-exponential kernel. The spatial correlation length,  $l_x$  is taken to be 3. For spatial discretization of the domain, the spectral/hp element method is used with  $N_e = 101$  and polynomial order 4 which results in the total points in the domain to be  $\bar{n} = 405$ . We impose stochastic Dirichlet boundary at  $x = 0$  given by,

$$u(0, t; \omega) = g(t; \omega).$$

Similar to the problem setup as the previous cases, the random process  $g(t; \omega)$  is taken as a function of the eigenvectors and singular values of the squared exponential kernel. The temporal correlation length is taken to be 3. The boundary conditions are taken to be,

$$g(t; \omega) = -\sin(2\pi t) + \sigma_t \sum_{i=1}^d \sqrt{\lambda_{t_i}} \varphi_i(t) \xi_i(\omega).$$



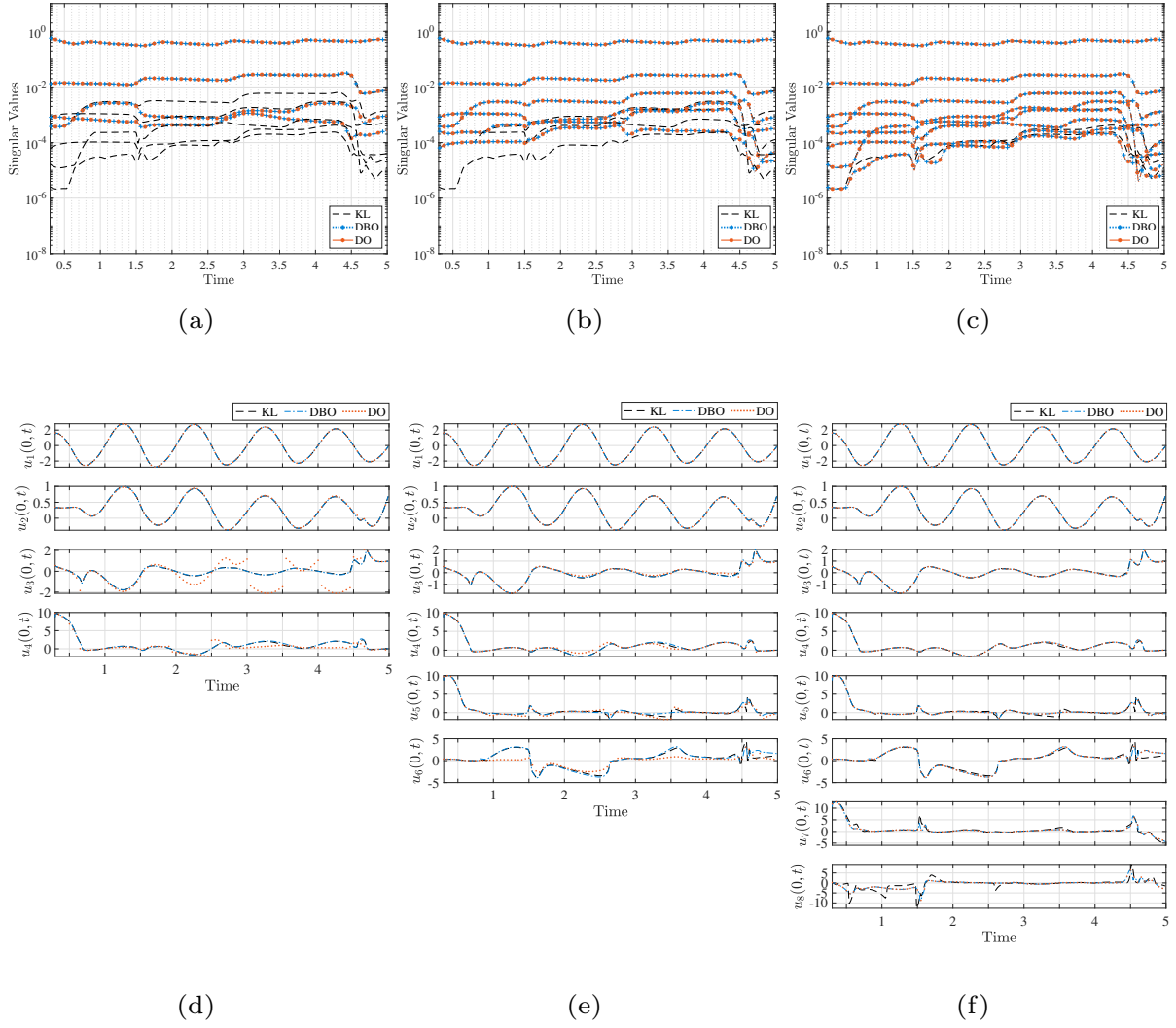


Figure 7: Burgers' equation: The first row shows the singular value comparison for KL, DBO and DO methods. The values are compared for three orders of reduction  $r = 4, 6$  and  $8$ . The evolution of the values of the modes at the left stochastic boundary are compared in the second row for the three methods.

Here,  $\sigma_t = 0.01$  and  $\xi \in \mathbb{R}^{n_s \times d}$  are discrete samples that are used for stochastic initial conditions. The initial conditions are given by,

$$u(x, 0; \omega) = \sin(2\pi x) + \sigma_x \sum_{i=1}^d \sqrt{\lambda_{x_i}} \psi_i(x) \xi_i(\omega).$$

The fourth-order Runge-Kutta method is used for time integration with  $\Delta t = 2.5 \times 10^{-4}$ . We use the technique of switching time at  $t_s = 0.3$  to initialize the spatial and stochastic modes. Although the switching time is used in cases where the initial conditions are deterministic, in this case for

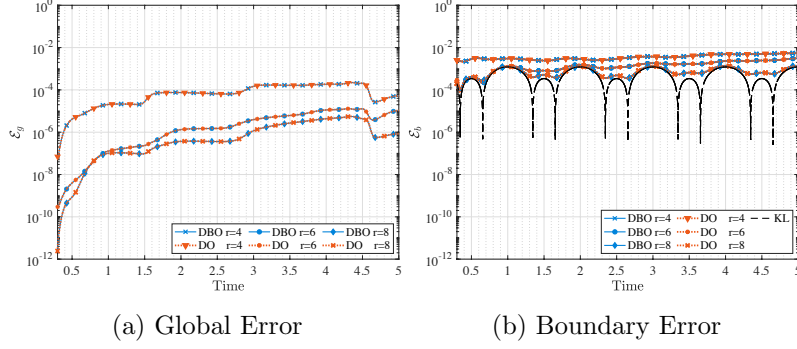


Figure 8: Burgers' equation: Error comparison for DBO and DO as compared with the KL solution. The global error i.e.,  $\mathcal{E}_g$  and the boundary error i.e.,  $\mathcal{E}_b$  are shown in (a) and (b) respectively.

$r = 8$ , the singular values for  $r > 6$  have negligible values and give rise to computational issues for inversion of the  $\Sigma$  matrix. The system is evolved till  $t_s = 0.3$  using PCM method to let the modes with lower singular values gain energy. The computed KL modes and singular values are used to initialize the DBO and DO spatial and stochastic modes at this time step. The system is then numerically evolved till  $t_f = 5$  using the DBO and DO methods. The results for three reduction orders  $r = 4, 6$  &  $8$  are shown in Fig.(7-8). The comparison of singular values is shown in first row of Fig.(7). The evolution of the modes at the stochastic boundary is shown in the second row of Fig.(7). For lower reduction orders, i.e.,  $r = 4, 6$ , the singular values and the evolution of the boundary modes show deviation from the KL solution. This error can be attributed to the unresolved modes in the solution. Although the random dimension is 4, the system cannot be exactly represented by 5 modes due to the non-linearity of the equation. The global and boundary error in the solution are shown in Fig.(8a-b). We observe that as the model reduction order is increased the error reduces for both DO and DBO. Since the solution cannot be represented exactly for  $r = 8$ , the KL and DBO show discrepancy in the boundary error as seen in Fig.(8b).

**3.3. 2D linear advection-diffusion equation.** The effect of stochastic boundary conditions is further demonstrated on a two dimensional forced convection heat transfer problem. We consider the linear advection-diffusion equation governed by:

$$(3.13) \quad \frac{\partial T}{\partial t} + (\mathbf{v} \cdot \nabla)T = \frac{1}{RePr} \nabla^2 T.$$

The velocity field  $\mathbf{v} = (u, v)$  is obtained by solving the 2D incompressible Navier-Stokes equation:

$$(3.14) \quad \frac{\partial \mathbf{v}}{\partial t} + (\mathbf{v} \cdot \nabla)\mathbf{v} = -\nabla p + \frac{1}{Re} \nabla^2 \mathbf{v},$$

where  $p$  is the pressure field,  $Re$  is the Reynolds number of the incompressible flow and  $Pr$  is the Prandtl number. For this case, the value of the Reynolds number and Prandtl number are taken to be  $Re = 3000$  and  $Pr = 1/300$  respectively. The schematic of the domain for this problem is shown in Fig.(9). The length of the bottom boundary is  $L = 10$ . The height of the domain is  $H = 5$ . The left and right boundary at  $x_1 = -5$  and  $x_1 = 5$  are taken to be outflow boundaries, i.e.,  $\partial T / \partial x_1 = 0$ . The velocity at the top inflow boundary is taken to be  $(u, v) = (0, -(1 - x_1^2 / 0.0625) \exp(-x_1^4 / 0.175^4) + 0.01 \sin(\pi x_1))$ . The small odd perturbation  $(0.01 \sin(\pi x_1))$

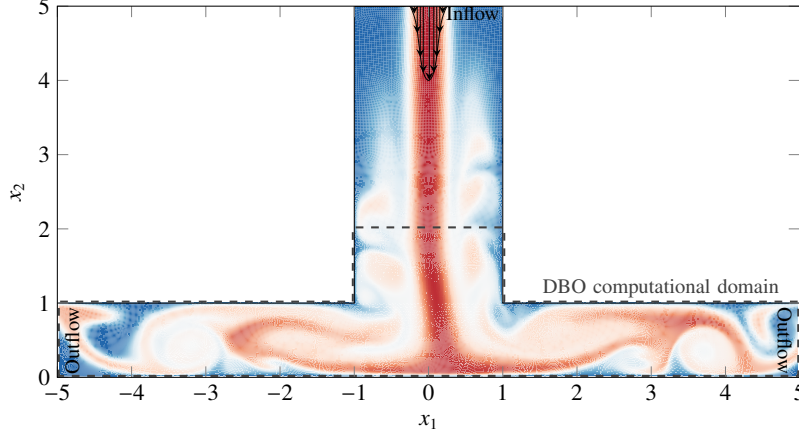


Figure 9: 2D forced convection: The figure shows the computational domain for the Nektar computations. The spectral element/hp simulation is used to compute the velocity field used to solve for the temperature equations using the DBO and DO methods. The dotted lines show the computational domain used for the DBO computations. An inflow boundary condition is enforced at  $x_2 = 5$ . Outflow boundary is enforced at  $x_1 = 5$  and  $x_1 = -5$ . All other boundaries are taken to be wall boundary ( $u, v = 0$ ).

is added to break the symmetry of the jet. The incompressible flow is solved using spectral/hp method with  $N_e = 4080$  and polynomial order 5 [51]. The  $(u, v)$  data from the incompressible solver is used for solving Eq.(3.13). To solve the temperature equation i.e., Eq.(3.13), the spatial domain is discretized by  $N_{e_{x_1}} = 51$ ,  $N_{e_{x_2}} = 31$  and polynomial order 4 which results in 205 points in the  $x_1$ -direction and 125 points in the  $x_2$ -direction. A stochastic Dirichlet boundary is introduced at the bottom wall with the temperature profile given by,

$$T(x_1, x_2 = 0, t; \omega) = g(x_1, t; \omega).$$

The random boundary condition is taken as;

$$g(x_1, t; \omega) = 1 + \sigma_{x_1} \sum_{n=1}^d \frac{1}{n^3} \frac{1}{\sqrt{L_{x_1}}} \cos\left(\frac{n\pi x_1}{L_{x_1}}\right) \sin\left(\frac{n\pi t}{L_t}\right) \xi_n,$$

here,  $L_{x_1}$  and  $L_t$  are taken to be 5 and  $\sigma_{x_1} = 0.05$ . The choice of the spatial modes depends on the boundary at  $(x_1, x_2) = (-5, 0)$  and  $(5, 0)$ . The spatial function  $\cos\left(\frac{n\pi x_1}{L_{x_1}}\right)$  ensures that the boundary at those points satisfy the Neumann boundary conditions imposed at the vertical outflow boundaries. The random space is taken to be  $d = 6$  dimensional. For this case,  $d = 6$  is taken as this approximation captures 99.99% of the random process. The 6-dimensional random space is discretized using the PCM quadrature points with 3 points in each random dimension. This results in the total number of samples to be  $n_s = 3^6 = 729$ . The temperature for all the other wall boundaries (except the bottom boundary) is set to be  $T = 0$ . The fourth-order Runge-Kutta method is used for time integration with  $\Delta t = 5 \times 10^{-4}$ . The system is evolved for  $t_f = 11$  Time Units and the  $t_s = 1$  is the switching time. Since the initial condition at  $t = 0$  is deterministic and the stochasticity has not evolved in the system, the SPDE is evolved till the switching time with the

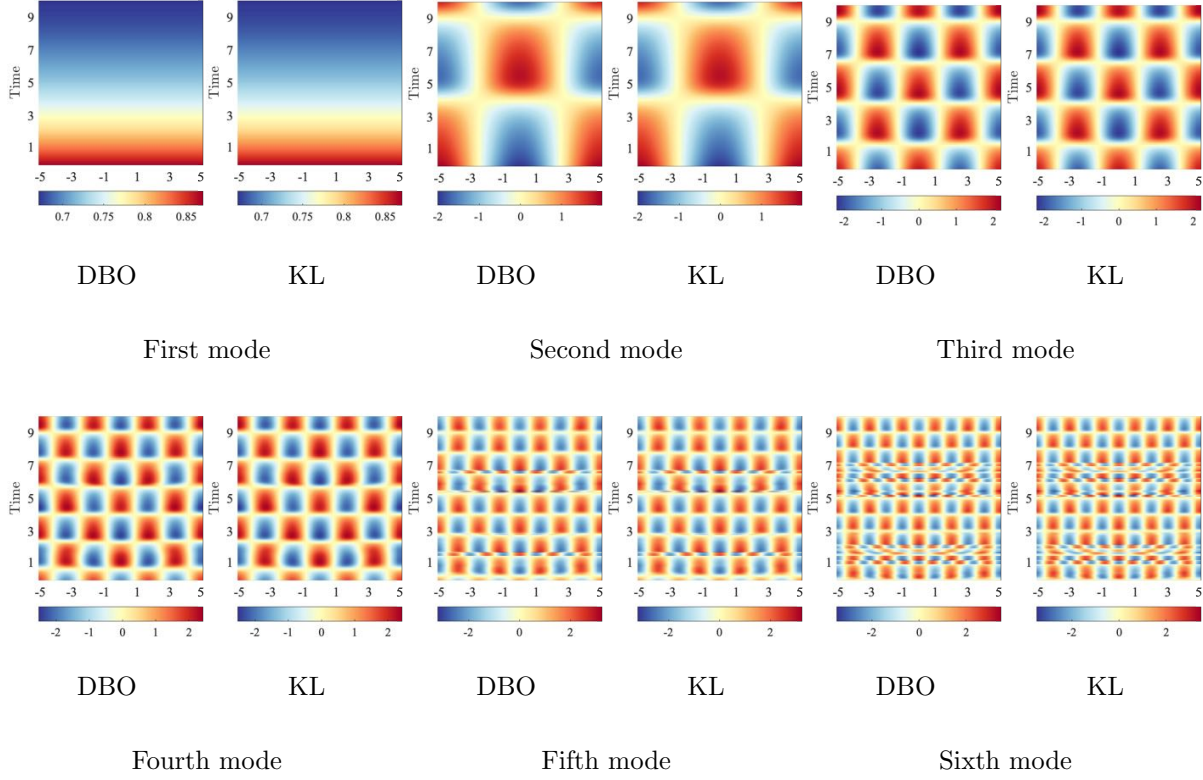


Figure 10: 2D forced convection: The evolution of the values of the modes at the stochastic Dirichlet boundary at  $x_2 = 0$  are compared for DBO and KL.

PCM samples and the KL decomposition of the solution at  $t = t_s$  is taken as the initial condition for the DBO and DO solvers. The singular values and the error of the solution are compared with the solution obtained by solving for the PCM samples. The singular value comparisons for three different reduction orders i.e.,  $r = 3, 5$  &  $7$  are shown in Fig.(11). The global and boundary errors for this case are plotted in Fig.(12). We observe that the errors decrease as the reduction order is increased. As it can be seen from the global and boundary errors for  $r = 9$ , DBO gives better accuracy than the DO due to the better condition number of the  $\Sigma$  inversion. We also observe that the DBO boundary error for  $r = 9$  is equal to the KL error. The evolution of the flow field for  $t = 2.5, 5, 7.5, 10$  of the tenth sample of the ME-PCM solution and the evolution of the spatial modes of the DBO solution are shown in Fig.(13). The values of the boundary modes for different time instances are represented in a surface plot in Fig.(10). Visual comparison shows that there is a good match between the KL and the DBO solution.

**3.4. 2D nonlinear advection-diffusion equation.** We lastly demonstrate the effect of stochastic boundary conditions on a two dimensional nonlinear equation. We consider the 2D advection-diffusion equation governed by:

$$(3.15) \quad \frac{\partial T}{\partial t} + (\mathbf{v} \cdot \nabla)T = \frac{1}{RePr} \nabla^2 T.$$

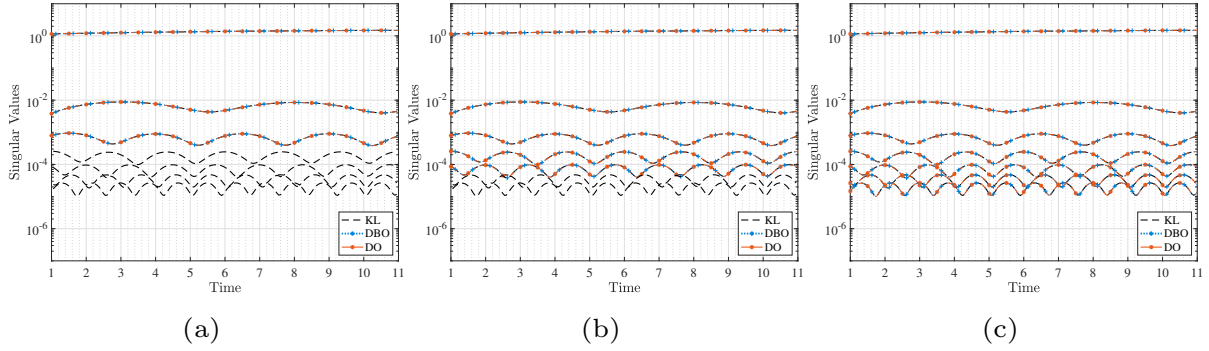


Figure 11: 2D forced convection: The singular value comparison for KL, DBO and DO methods is shown. The values are compared for three orders of reduction  $r = 3, 5$  &  $7$ .

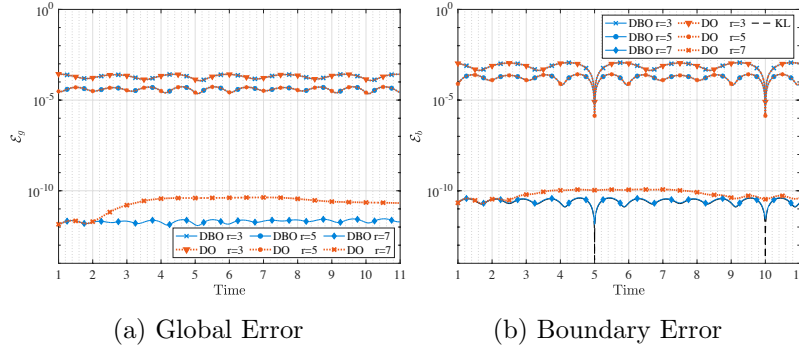


Figure 12: 2D forced convection: Error comparison for DBO and DO as compared with the KL solution. The figure on the left shows the comparison in the  $\mathcal{E}_g$ , i.e., global error. The figure on the right shows the comparison for the  $\mathcal{E}_b$ , i.e., boundary error.

The velocity field  $\mathbf{v} = (u, v)$  is obtained by solving the 2D incompressible Navier-Stokes equation i.e, Eq.(3.14). The Prandtl number for this case however, is taken to be temperature dependent:  $Pr = f(T)$ , which makes the governing equation nonlinear. Here, we take Prandtl number to be  $Pr = \frac{1}{300(\alpha + \beta T)}$ . For this case,  $\alpha = 1$  and  $\beta = 0.9$ . The Reynolds number is  $Re = 3000$ . The schematic of the problem is same as the previous case. The bottom boundary condition is prescribed by stochastic Dirichlet temperature according to:

$$T(x_1, x_2 = 0; \omega) = g(x_1; \omega)$$

$$g(x_1; \omega) = 1 + \sigma_{x_1} \sum_{n=1}^d \frac{1}{n} \frac{1}{\sqrt{L_{x_1}}} \cos\left(\frac{n\pi x_1}{L_{x_1}}\right) \xi_n,$$

where  $L_{x_1}$  and  $L_t$  are taken to be 5 and  $\sigma_{x_1} = 0.5$ . The Dirichlet boundary conditions for this case are taken to be time-independent. The singular values for this case are compared in Fig.(15). The singular values are compared for three different reduction orders,  $r = 5, 7$  and  $9$ . The error comparison for this case is plotted in Fig.(14). We observe that the errors improve for both DBO



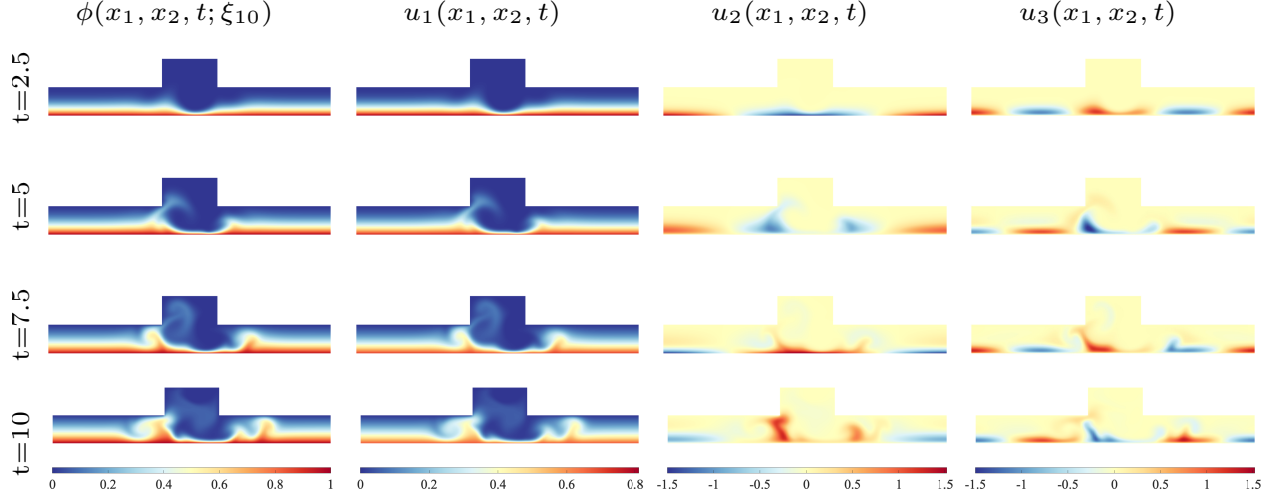


Figure 13: 2D forced convection: Evolution of the first three spatial modes is shown for  $t = 2.5, 5, 7.5, 10$ . The first column shows the solution obtained for different time snapshots for the tenth sample. The next three columns show the evolution of the spatial modes as the flow field evolves.

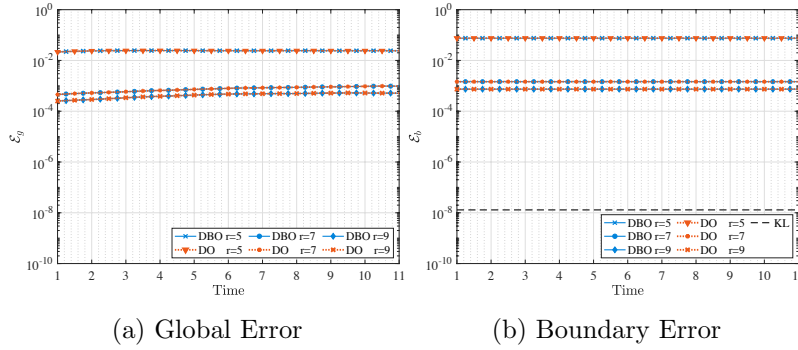


Figure 14: 2D forced convection with temperature dependent conductivity: Error comparison for DBO and DO as compared with the KL solution. The figure on the left shows the comparison in the  $\mathcal{E}_g$ , i.e., global error. The figure on the right shows the comparison for the  $\mathcal{E}_b$ , i.e., boundary error.

and DO as the order of reduction is increased. For the linear case, when  $d = 6$  we observe that  $r = 7$  can define the system exactly. However, for the nonlinear case, we observe that modes 8 and 9 also have non-negligible singular values and that these values pick up energy as the system evolves.

**4. Conclusions.** In this paper, we present a methodology for determine the boundary conditions of time-dependent bases for SPDEs with stochastic boundary conditions. We present the formulation for both DBO and DO formulations. The presented methodology is informed by the fact that the DBO and DO evolution equations are first-order optimality conditions of their respective variational principles. We leverage the variational principle to derive evolution equation

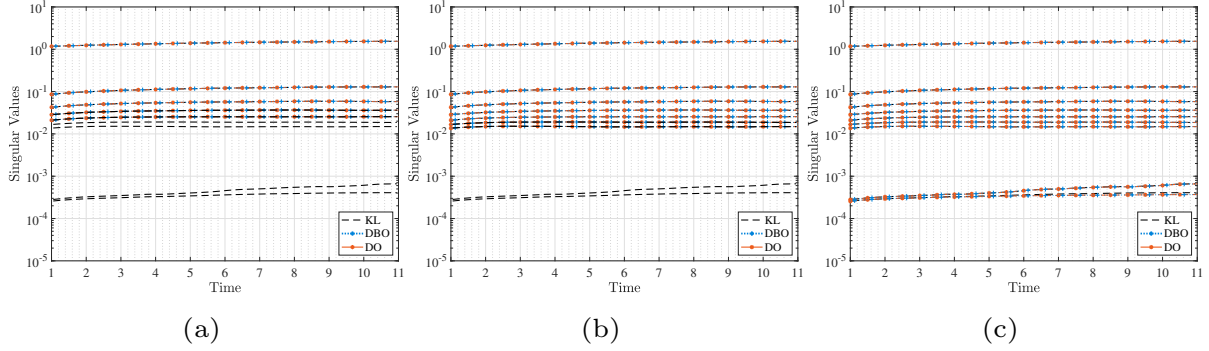


Figure 15: 2D forced convection with temperature dependent conductivity: The singular value comparison for KL, DBO and DO methods is shown. The values are compared for three orders of reduction  $r = 5, 7$  and  $9$

for value of spatial modes at the boundaries. The methodology enables determining the value at a stochastic boundary for the spatial modes at no additional computational cost than that of solving the same SPDE but with homogeneous boundary condition. For a high dimensional random boundary, the number of modes need not increase with the random dimensions thus enabling the application of the presented methodology to problems with high-dimensional stochastic boundary conditions. The method is developed for stochastic Dirichlet, Neumann, and Robin boundary conditions.

The method is applied to one dimensional linear advection-diffusion equation for three different boundary conditions. The error comparison for the method is presented for two methods DBO and DO and three reduction orders. The solution is compared to the instantaneous KL solution. We observe that the DBO method performs better in the absence of unresolved modes of the system or when the order of reduction defines the system exactly. This can be attributed to the better condition number of the  $\Sigma$  matrix or the factorization of the covariance matrix.

The method is also applied to stochastic one dimensional Burgers' equation for stochastic Dirichlet boundary. The results for DBO and DO are presented for three different reduction orders. In this case, due to the error from the unresolved modes being greater than the error in DO from the inversion of the covariance matrix, both the methods show same order of error with respect to the KL solution.

Lastly, the method is applied to two dimensional advection-diffusion problem. We consider two cases for this equation, for the first case the conduction coefficient is kept constant making the equation linear and for the second case, the conduction coefficient has a linear temperature dependence, making the equation weakly nonlinear. The error comparison and the evolution of the modes at the boundary are compared. It is observed that both the DO and DBO methods show similar levels of accuracy.

**Acknowledgments.** This work has been supported by Air Force Office of Scientific Research award (PM: Dr. Fariba Fahroo) FA9550-21-1-0247 and by the National Science Foundation (NSF), USA under Grant No. 2042918. This research was supported in part by the University of Pittsburgh Center for Research Computing through the resources provided.

## References.

- [1] P. Patil and H. Babae, “Real-time reduced-order modeling of stochastic partial differential equations via time-dependent subspaces,” *Journal of Computational Physics*, p. 109511, 2020.
- [2] T. P. Sapsis and P. F. Lermusiaux, “Dynamically orthogonal field equations for continuous stochastic dynamical systems,” *Physica D: Nonlinear Phenomena*, vol. 238, no. 23-24, pp. 2347–2360, 2009.
- [3] M. B. Giles, “Multilevel Monte Carlo path simulation,” *Operations Research*, vol. 56, no. 3, pp. 607–617, 2008.
- [4] A. Barth, C. Schwab, and N. Zollinger, “Multi-level Monte Carlo Finite Element method for elliptic PDEs with stochastic coefficients,” *Numerische Mathematik*, vol. 119, no. 1, pp. 123–161, 2011.
- [5] F. Y. Kuo, C. Schwab, and I. H. Sloan, “Quasi-Monte Carlo finite element methods for a class of elliptic partial differential equations with random coefficients,” *SIAM Journal on Numerical Analysis*, vol. 50, no. 6, pp. 3351–3374, 2012.
- [6] R. Chen and J. S. Liu, “Mixture Kalman filters,” *Journal of the Royal Statistical Society: Series B (Statistical Methodology)*, vol. 62, no. 3, pp. 493–508, 2000.
- [7] R. Van Der Merwe and E. Wan, “Gaussian mixture sigma-point particle filters for sequential probabilistic inference in dynamic state-space models,” in *2003 IEEE International Conference on Acoustics, Speech, and Signal Processing, 2003. Proceedings.(ICASSP’03).*, vol. 6, pp. VI–701, IEEE, 2003.
- [8] R. G. Ghanem and P. D. Spanos, *Stochastic finite elements: A spectral approach*. Courier Corporation, 2003.
- [9] X. Wan and G. E. Karniadakis, “Multi-element generalized polynomial chaos for arbitrary probability measures,” *SIAM Journal on Scientific Computing*, vol. 28, no. 3, pp. 901–928, 2006.
- [10] D. Xiu and J. S. Hesthaven, “High-order collocation methods for differential equations with random inputs,” *SIAM Journal on Scientific Computing*, vol. 27, no. 3, pp. 1118–1139, 2005.
- [11] D. Xiu and G. E. Karniadakis, “The Wiener-Askey polynomial chaos for stochastic differential equations,” *SIAM Journal on Scientific Computing*, vol. 24, no. 2, pp. 619–644, 2002.
- [12] J. Foo and G. E. Karniadakis, “Multi-element probabilistic collocation method in high dimensions,” *Journal of Computational Physics*, vol. 229, no. 5, pp. 1536–1557, 2010.
- [13] J. Foo, X. Wan, and G. E. Karniadakis, “The multi-element probabilistic collocation method (ME-PCM): Error analysis and applications,” *Journal of Computational Physics*, vol. 227, no. 22, pp. 9572–9595, 2008.
- [14] I. Babuška, F. Nobile, and R. Tempone, “A stochastic collocation method for elliptic partial differential equations with random input data,” *SIAM Journal on Numerical Analysis*, vol. 45, no. 3, pp. 1005–1034, 2007.
- [15] B. Ganapathysubramanian and N. Zabaras, “Sparse grid collocation schemes for stochastic natural convection problems,” *Journal of Computational Physics*, vol. 225, no. 1, pp. 652–685, 2007.
- [16] X. Yang, M. Choi, G. Lin, and G. E. Karniadakis, “Adaptive ANOVA decomposition of stochastic incompressible and compressible flows,” *Journal of Computational Physics*, vol. 231, no. 4, pp. 1587–1614, 2012.
- [17] H. Babae, X. Wan, and S. Acharya, “Effect of uncertainty in blowing ratio on film cooling effectiveness,” *Journal of Heat Transfer*, vol. 136, no. 3, 2014.
- [18] D. Zhang, H. Babae, and G. E. Karniadakis, “Stochastic domain decomposition via moment minimization,” *SIAM Journal on Scientific Computing*, vol. 40, no. 4, pp. A2152–A2173, 2018.

- [19] P. Frauenfelder, C. Schwab, and R. A. Todor, "Finite elements for elliptic problems with stochastic coefficients," *Computer Methods in Applied Mechanics and Engineering*, vol. 194, no. 2-5, pp. 205–228, 2005.
- [20] H. G. Matthies and A. Keese, "Galerkin methods for linear and nonlinear elliptic stochastic partial differential equations," *Computer Methods in Applied Mechanics and Engineering*, vol. 194, no. 12-16, pp. 1295–1331, 2005.
- [21] C. Schwab and R.-A. Todor, "Sparse finite elements for elliptic problems with stochastic loading," *Numerische Mathematik*, vol. 95, no. 4, pp. 707–734, 2003.
- [22] O. P. L. Maître, O. M. Knio, H. N. Najm, and R. G. Ghanem, "A stochastic projection method for fluid flow. I: Basic formulation," *Journal of Computational Physics*, vol. 173, no. 2, pp. 481–511, 2001.
- [23] M. Jardak, C.-H. Su, and G. E. Karniadakis, "Spectral polynomial chaos solutions of the stochastic advection equation," *Journal of Scientific Computing*, vol. 17, no. 1-4, pp. 319–338, 2002.
- [24] D. Xiu and G. E. Karniadakis, "Modeling uncertainty in flow simulations via generalized polynomial chaos," *Journal of Computational Physics*, vol. 187, no. 1, pp. 137–167, 2003.
- [25] A. J. Chorin, "Gaussian fields and random flow," *Journal of Fluid Mechanics*, vol. 63, no. 1, pp. 21–32, 1974.
- [26] O. M. Knio and O. Le Maître, "Uncertainty propagation in CFD using polynomial chaos decomposition," *Fluid Dynamics Research*, vol. 38, no. 9, p. 616, 2006.
- [27] S. Das, R. Ghanem, and S. Finette, "Polynomial chaos representation of spatio-temporal random fields from experimental measurements," *Journal of Computational Physics*, vol. 228, no. 23, pp. 8726–8751, 2009.
- [28] X. Wan and G. E. Karniadakis, "Long-term behavior of polynomial chaos in stochastic flow simulations," *Computer Methods in Applied Mechanics and Engineering*, vol. 195, no. 41-43, pp. 5582–5596, 2006.
- [29] M. Branicki and A. J. Majda, "Fundamental limitations of polynomial chaos for uncertainty quantification in systems with intermittent instabilities," *Communications in Mathematical Sciences*, vol. 11, no. 1, pp. 55–103, 2013.
- [30] C. Pettit and P. Beran, "Spectral and multiresolution Wiener expansions of oscillatory stochastic processes," *Journal of Sound and Vibration*, vol. 294, no. 4-5, pp. 752–779, 2006.
- [31] T. P. Sapsis, *Dynamically orthogonal field equations for stochastic fluid flows and particle dynamics*. PhD thesis, Massachusetts Institute of Technology, 2011.
- [32] H. Babae, M. Choi, T. P. Sapsis, and G. E. Karniadakis, "A robust bi-orthogonal/dynamically-orthogonal method using the covariance pseudo-inverse with application to stochastic flow problems," *Journal of Computational Physics*, vol. 344, pp. 303–319, 2017.
- [33] M. Cheng, T. Y. Hou, and Z. Zhang, "A dynamically bi-orthogonal method for time-dependent stochastic partial differential equations I: Derivation and algorithms," *Journal of Computational Physics*, vol. 242, pp. 843–868, 2013.
- [34] M. Cheng, T. Y. Hou, and Z. Zhang, "A dynamically bi-orthogonal method for time-dependent stochastic partial differential equations II: Adaptivity and generalizations," *Journal of Computational Physics*, vol. 242, pp. 753–776, 2013.
- [35] M. Choi, T. P. Sapsis, and G. E. Karniadakis, "On the equivalence of dynamically orthogonal and bi-orthogonal methods: Theory and numerical simulations," *Journal of Computational Physics*, vol. 270, pp. 1–20, 2014.
- [36] H. Babae, "An observation-driven time-dependent basis for a reduced description of transient

- stochastic systems,” *Proceedings of the Royal Society A*, vol. 475, no. 2231, p. 20190506, 2019.
- [37] H. Babaei and T. Sapsis, “A minimization principle for the description of modes associated with finite-time instabilities,” *Proceedings of the Royal Society A: Mathematical, Physical and Engineering Sciences*, vol. 472, no. 2186, p. 20150779, 2016.
- [38] H. Babaei, M. Farazmand, T. Sapsis, and G. Haller, “Computing finite-time lyapunov exponents with optimally time dependent reduction,” in *APS Division of Fluid Dynamics Meeting Abstracts*, pp. L8–003, 2016.
- [39] H. Babaei, M. Farazmand, G. Haller, and T. P. Sapsis, “Reduced-order description of transient instabilities and computation of finite-time lyapunov exponents,” *Chaos: An Interdisciplinary Journal of Nonlinear Science*, vol. 27, no. 6, p. 063103, 2017.
- [40] A. Blanchard, S. Mowlavi, and T. P. Sapsis, “Control of linear instabilities by dynamically consistent order reduction on optimally time-dependent modes,” *Nonlinear Dynamics*, vol. 95, no. 4, pp. 2745–2764, 2019.
- [41] T. P. Sapsis, “New perspectives for the prediction and statistical quantification of extreme events in high-dimensional dynamical systems,” *Philosophical Transactions of the Royal Society A: Mathematical, Physical and Engineering Sciences*, vol. 376, no. 2127, p. 20170133, 2018.
- [42] M. Donello, M. Carpenter, and H. Babaei, “Computing sensitivities in evolutionary systems: A real-time reduced order modeling strategy,” *arXiv preprint arXiv:2012.14028*, 2020.
- [43] A. Nouri, H. Babaei, P. Givi, H. Chelliah, and D. Livescu, “Skeletal model reduction with forced optimally time dependent modes,” *Combustion and Flame*, p. 111684, 2021.
- [44] D. Ramezani, A. G. Nouri, and H. Babaei, “On-the-fly reduced order modeling of passive and reactive species via time-dependent manifolds,” *Computer Methods in Applied Mechanics and Engineering*, vol. 382, p. 113882, 2021.
- [45] M. H. Beck, A. Jäckle, G. A. Worth, and H.-D. Meyer, “The multiconfiguration time-dependent Hartree (MCTDH) method: a highly efficient algorithm for propagating wavepackets,” *Physics reports*, vol. 324, no. 1, pp. 1–105, 2000.
- [46] C. Bardos, F. Golse, A. D. Gottlieb, and N. J. Mauser, “Mean field dynamics of fermions and the time-dependent Hartree–Fock equation,” *Journal de mathématiques pures et appliquées*, vol. 82, no. 6, pp. 665–683, 2003.
- [47] O. Koch and C. Lubich, “Dynamical low-rank approximation,” *SIAM Journal on Matrix Analysis and Applications*, vol. 29, no. 2, pp. 434–454, 2007.
- [48] O. Koch and C. Lubich, “Dynamical tensor approximation,” *SIAM Journal on Matrix Analysis and Applications*, vol. 31, no. 5, pp. 2360–2375, 2010.
- [49] E. Musharbash and F. Nobile, “Dual dynamically orthogonal approximation of incompressible Navier Stokes equations with random boundary conditions,” *Journal of Computational Physics*, vol. 354, pp. 135–162, 2018.
- [50] X. Wan and G. E. Karniadakis, “An adaptive multi-element generalized polynomial chaos method for stochastic differential equations,” *Journal of Computational Physics*, vol. 209, no. 2, pp. 617–642, 2005.
- [51] G. E. Karniadakis and S. J. Sherwin, *Spectral/hp element methods for computational fluid dynamics*. Oxford University Press, USA, 2005.